CHIN. PHYS. LETT. Vol. 39, No. 3 (2022) 037301 Review

Recent Advances in Moiré Superlattice Structures of Twisted Bilayer and Multilayer Graphene

Xiao-Feng Li(黎晓峰)[1], Ruo-Xuan Sun(孙若轩)[1], Su-Yun Wang(王苏云)[1], Xiao Li(李潇)[2], Zhi-Bo Liu(刘智波)[1,3,4*], and Jian-Guo Tian(田建国)[1,3,4]

[1]*The Key Laboratory of Weak Light Nonlinear Photonics (Ministry of Education), School of Physics and Teda Applied Physics Institute, Nankai University, Tianjin 300071, China*
[2]*Department of Physics, City University of Hong Kong, Kowloon, Hong Kong, China*
[3]*Renewable Energy Conversion and Storage Center, Nankai University, Tianjin 300071, China*
[4]*The Collaborative Innovation Center of Extreme Optics, Shanxi University, Taiyuan 030006, China*

(Received 20 December 2021; accepted 25 January 2022; published online 1 March 2022)

Twisted bilayer graphene (TBG), which has drawn much attention in recent years, arises from van der Waals materials gathering each component together via van der Waals force. It is composed of two sheets of graphene rotated relatively to each other. Moiré potential, resulting from misorientation between layers, plays an essential role in determining the band structure of TBG, which directly relies on the twist angle. Once the twist angle approaches a certain critical value, flat bands will show up, indicating the suppression of kinetic energy, which significantly enhances the importance of Coulomb interaction between electrons. As a result, correlated states like correlated insulators emerge from TBG. Surprisingly, superconductivity in TBG is also reported in many experiments, which drags researchers into thinking about the underlying mechanism. Recently, the interest in the atomic reconstruction of TBG at small twist angles comes up and reinforces further understandings of properties of TBG. In addition, twisted multilayer graphene receives more and more attention, as they could likely outperform TBG although they are more difficult to handle experimentally. In this review, we mainly introduce theoretical and experimental progress on TBG. Besides the basic knowledge of TBG, we emphasize the essential role of atomic reconstruction in both experimental and theoretical investigations. The consideration of atomic reconstruction in small-twist situations can provide us with another aspect to have an insight into physical mechanism in TBG. In addition, we cover the recent hot topic, twisted multilayer graphene. While the bilayer situation can be relatively easy to resolve, multilayer situations can be really complicated, which could foster more unique and novel properties. Therefore, in the end of the review, we look forward to future development of twisted multilayer graphene.

DOI: 10.1088/0256-307X/39/3/037301

1. Introduction. The discovery of graphene opened a new era of two-dimensional materials.[1] Since then, there has appeared an explosive increase of research on graphene. Meanwhile, researchers have dug out more two-dimensional materials under the enlightenment of graphene, including molybdenum disulfide (MoS_2),[2] palladium diselenide ($PdSe_2$),[3] tungsten disulfide (WS_2),[4] tungsten diselenide (WSe_2),[5] vanadium diselenide (VSe_2),[6] and so forth, which enrich the whole family. Since the peculiarity of two-dimensional materials enables researchers to combine different species together to form different van der Waals stacked materials as they wish, large amounts of novel structures arise from different assemblies of two-dimensional materials, where researchers have found amazing properties such as inter- and intralayer excitons,[7–13] interlayer magnetic orders,[14] correlated insulating states and superconducting domes in transport measurement.[15–20] Till now, researchers are still attempting to construct various stacking structures with potential astonishing properties. Twisted bilayer graphene is a crucial research field in van der Waals materials.

In the past decade, researchers built a continuum model (the BM model) to describe the low energy physics of TBG,[21] to which researchers have paid much attention. Then the dependence of Fermi velocity on twist angle is investigated and flat bands are discovered at a certain critical angle. The existence of flat bands indicates the peak density of states, which highlights the importance of interactions between electrons given that their kinetic energies are perfectly suppressed. Correlated insulators and superconductors[22–25] have been widely reported on TBG. There is no doubt that TBG provides a platform to observe and understand highly correlated phases. The intricate electron behaviors under magnetic field were also studied.[26] What is more, adjustable moiré

*Corresponding author. Email: liuzb@nankai.edu.cn
© 2022 Chinese Physical Society and IOP Publishing Ltd

potential in TBG fascinates researchers to design more sophisticated structure to obtain expected properties, including adding more graphene layers.[27–32] However, the realistic situation of twisted graphene system can be very subtle and complicated due to the existence of atomic reconstruction, which can be identified through experimental characterization methods. This has risen up as a research hotspot recently. This review will focus on the properties of TBG. This paper will be organized as follows: in section 1, we introduce the basic structure of TBG and some relevant optical properties, then mention the continuum model which appropriately describes the low energy physics of TBG. In section 2, we discuss the important structural deformation occurring in TBG in details. Then in section 3, characterization method and experimental observations of moiré supercell are introduced. In section 4, we mainly include unique properties of TBG. Finally in section 5, we cover a new direction for graphene-based moiré systems, twisted multilayer graphene.

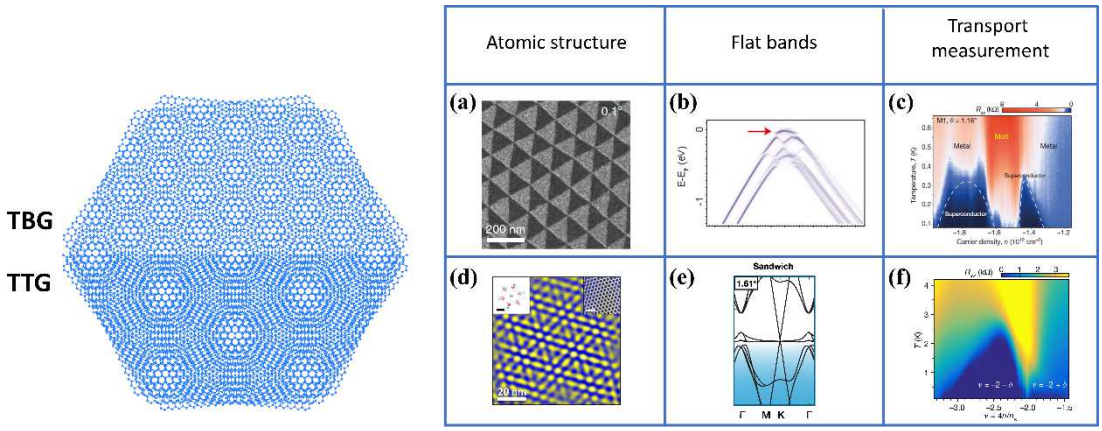

Fig. 1. (a) Transmission electron microscope (TEM) dark-field images of twist graphene (reproduced with permission from Ref. [33]). (b) Nano angle resolved photoemission (Nano ARPES) result of TBG along different cuts in momentum space. The flat bands are marked by red arrows (reproduced with permission from Ref. [34]). (c) Longitudinal resistance of TBG as a function of carrier density and temperature. Superconducting domes and correlated insulating regimes can be obviously found (reproduced with permission from Ref. [35]). (d) Scanning tunneling microscope (STM) topography of consecutively twisted trilayer graphene (CTTG). Top left inset shows the fast Fourier transform images of STM results. Top right inset shows a 2 nm × 2 nm STM image of CTTG with honeycomb lattice (reproduced with permission from Ref. [36]). (e) Band structure of 1.61° middle-layer-twisted trilayer graphene (MTTG) (reproduced with permission from Ref. [29]). (f) Superconducting domes in transport measurement of ∼1.57° MTTG (reproduced with permission from Ref. [30]).

2. Basic Structure of Twisted Graphene—2.1. Geometry of TBG. The first thing to understand for the physics of TBG is building the basic structure. First, we turn to the basic component of TBG, single-layer graphene (SLG). As is known, in SLG there are two sublattices called A and B here, which construct the so-called 'honeycomb' periodic pattern. The positions of sublattice A can be definite by two vectors $\boldsymbol{a}_1 = \left(\frac{1}{2}, \frac{\sqrt{3}}{2}\right) a_0$, $\boldsymbol{a}_2 = \left(-\frac{1}{2}, \frac{\sqrt{3}}{2}\right) a_0$ in real space, where a_0 is the lattice constant of graphene, while the other sublattice B can be obtained by translating all A sublattices by $\boldsymbol{d} = (2\boldsymbol{a}_1 - \boldsymbol{a}_2)/3$, which is shown in Fig. 2(a).

The reciprocal vector of periodic structure can be easily gained by the relation $\boldsymbol{a}_i \cdot \boldsymbol{b}_j = 2\pi\delta_{ij}$. Then we can get the reciprocal vectors of graphene: $b_1 = \left(\frac{\sqrt{3}}{2}, \frac{1}{2}\right) \frac{4\pi}{\sqrt{3}a_0}$, $b_2 = \left(-\frac{\sqrt{3}}{2}, \frac{1}{2}\right) \frac{4\pi}{\sqrt{3}a_0}$, which define the corresponding momentum lattice. Just as shown in Fig. 2(b), there are also two inequivalent Dirac points referred to as K and K' within the first Brillouin zone, which originate from two sublattices in real space.

The Hamiltonian of SLG is given by

$$H(\boldsymbol{k}) = -t \begin{pmatrix} 0 & g(\boldsymbol{k}) \\ g^*(\boldsymbol{k}) & 0 \end{pmatrix}, \tag{1}$$

where $-t$ is the hopping magnitude and $g(\boldsymbol{k}) = e^{i\boldsymbol{k}\cdot\boldsymbol{d}}(1+e^{-i\boldsymbol{k}\cdot\boldsymbol{a}_1}+e^{-i\boldsymbol{k}\cdot\boldsymbol{a}_2})$ reflects the hopping process between one site and its nearest neighbors. Once we diagonalize the Hamiltonian, we can get the dispersion relation as

$$E(\boldsymbol{k}) = \pm t\Big[4\cos\left(\frac{1}{2}a_0k_x\right)\cos\left(\frac{\sqrt{3}}{2}a_0k_y\right) + 2\cos\left(a_0k_x\right) + 3\Big]^{1/2}, \tag{2}$$

which is depicted in Fig. 2(c). Generally, we are only concerned with the low-energy physics of graphene, so the Hamiltonian above can be expanded around the Dirac point as

$$H_{\mathrm{SLG}} = v \begin{pmatrix} 0 & \pm p_x - ip_y \\ \pm p_x + ip_y & 0 \end{pmatrix} = v\boldsymbol{\sigma}\cdot\boldsymbol{p}. \tag{3}$$

Here, $\boldsymbol{p} = \hbar\boldsymbol{q}$, with $\boldsymbol{q}$ being the wavevector measured from the Dirac point; $\boldsymbol{\sigma} = (\pm\sigma_x, \sigma_y)$ is Pauli matrices with $\pm$ denoting different valleys. More details about the band structure of SLG based on the tight-binding model can be accessed in Ref. [37] and other references.[38,39]

Apart from intuitive band structures, characterization of density of states (DOS) of band structures can also work as a useful method to have insight into electronic properties. DOS at energy E is defined as

$$\mathrm{DOS}\,[E] = 2\sum_{k\in \mathrm{BZ},\gamma} \delta\left(E - E_\gamma\left(k\right)\right), \tag{4}$$

where $E_\gamma(k)$ is the dispersion, with γ the band index. Factor 2 accounts for the spin degeneracy without loss of generality; δ is Dirac delta function. With this definition, numerical results of DOS for an SLG system can be obtained as shown in Fig. 2(e) after choosing a reasonable energy window. There are two obvious symmetric peaks in the DOS spectrum, which can be attributed to the saddle point referred to as van Hove singularity (VHS) in the band structure. The appearance of VHS originates from interaction between electrons, highly depending on the interlayer interaction, which is why there is no sign of VHSs in the decoupled TBG.[40]

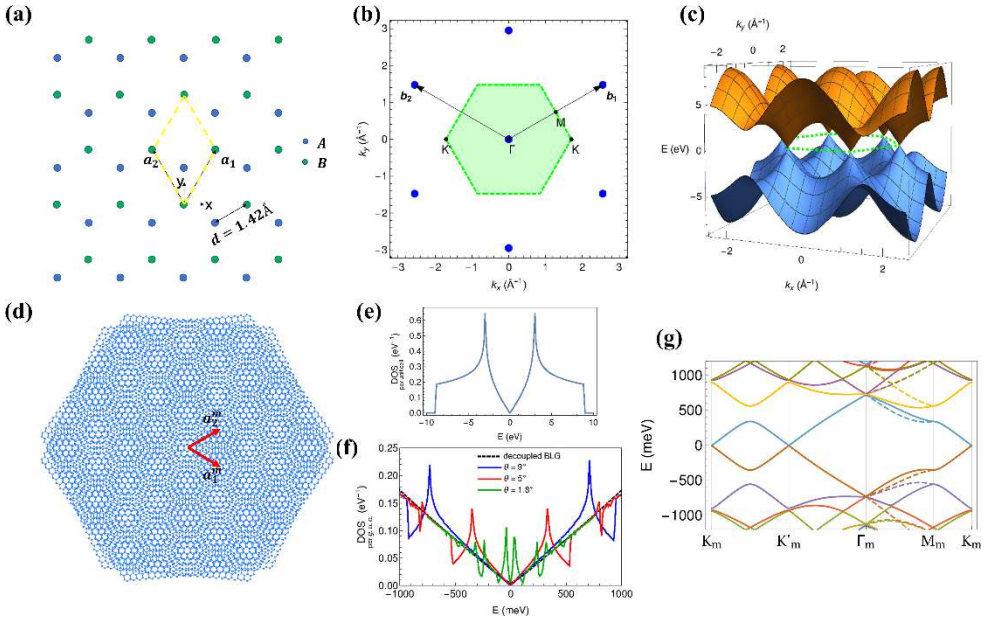

Fig. 2. (a) Basic structure of SLG. (b) Brillouin zone of SLG. (c) Band structure of SLG. (d) Moiré pattern formed by interlayer twist between two sheets of graphene. (e) Density of states of SLG in a specific energy range. (f) Density of states for TBG with different twist angles 9°, 5°, and 1.8°. (g) Electronic band structure of TBG with twist angle 5°. [(b), (c), (e), (f), (g)] Reproduced with permission from Ref. [41].

Then it comes to constructing TBG. For two sheets of graphene, there are four kinds of sublattices A_i, B_i within a unit cell, where i is the layer index. When we start with AA-stacked bilayer graphene, where each site in the top layer is aligned with its counterpart in the bottom layer, we can take an axis which goes through two vertically aligned A(B) sublattices and rotate the top layer around this axis by a specific angle, then we will get TBG. Although the manipulation is simple theoretically, the main difficulty arises from the tiny size and unclean surface of sample because of the immature of synthesis techniques. Contemporarily, researchers are still struggling to both develop a new method of synthesizing large-size graphene and increase the accuracy of twist angles.[42,43]

The structure we get from the above rotation manipulation can then be divided into two kinds of situations, incommensurate structure and commensurate structure, which differ in whether to remain periodic after rotation of the top layer. The method to distinguish periodic structures of TBG relies on geometric analysis dependent on twist angle. Here we list two methods developed by Lopes dos Santos *et al.*[44] and Shallcross *et al.*[45]

The commensurate angle which can create periodic TBG structure is[44]

$$\cos\theta = \frac{3m^2 + 3mr + \frac{r^2}{2}}{3m^2 + 3mr + r^2}, \tag{5}$$

where m and r are coprime positive integers, and $0 < \theta < \pi/3$; or[45]

$$\theta = \cos^{-1}\left(\frac{3q^2 - p^2}{3q^2 + p^2}\right), \tag{6}$$

with $pq \in Z$ and for $p \geqslant q$, $0 < \theta < \pi/3$.

From the expression we can know that the commensurate angles are discrete and most populated near 0° and 60°, which is demonstrated in Fig. 3(a) including the symmetry of commensurate distribution.

At these commensurate angles, spatial periodic structure can be formed and exhibit the so-called "moiré" pattern as shown in Fig. 2(d), where a_1^m, a_2^m are the vectors of superlattice, and their lengths are dependent on the twist angle θ,

$$|a_1^m| = \frac{a_0}{2\sin(\theta/2)}. \tag{7}$$

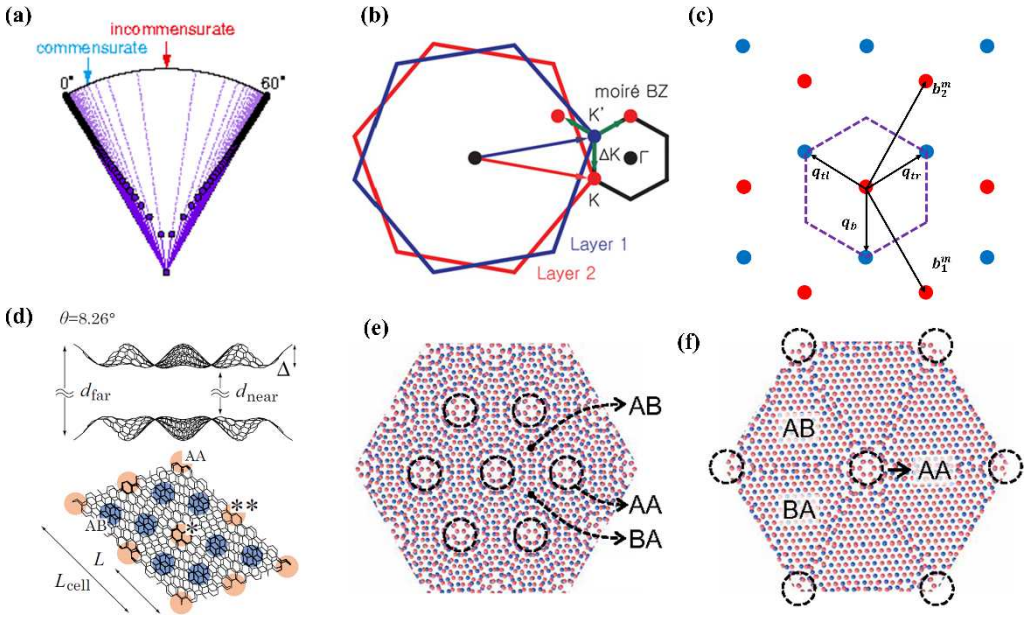

Fig. 3. (a) Distribution of commensurate and incommensurate angles. The length of solid line represents the length of moiré period (reproduced with permission from Ref. [46]). (b) Formation of moiré Brillouin zone. Red and blue hexagonal zones are original SLG's Brillouin zones from two layers, which are rotated clockwise and counterclockwise, respectively. ΔK is the momentum difference between two Dirac points, which can be controlled by the twist angle. Γ is the center of moiré Brillouin zone (reproduced with permission from Ref. [47]). (c) Coupling between states from two layers. Here b_{1m} and b_{2m} are reciprocal vectors of moiré Brillouin zone. (d) Interlayer distances at different stacking regions and spatial demonstration (reproduced with permission from Ref. [48]). (e) Stacking configurations in real space. AA, AB and BA stand for AA-, AB-, BA stacking order in TBG. (f) Spatial distribution of stacking order after atomic reconstruction. [(e), (f)] Reproduced with permission from Ref. [49].

Specifically, the commensurate angle can be further divided into two types based on the relationship between r and 3 in Eq. (5). Use $\gcd(r, s)$ to represent the greatest common divisor of r and s, then:

(1) If $\gcd(r, 3)$=3, in the primitive cell of TBG, A_1, B_1 sublattices and hexagon center H_1 of top layer are aligned with A_2, B_2 sublattices and hexagon center H_2 of bottom layer, respectively. This situation is called the sublattice exchange even (SE-even).[50]

(2) If $\gcd(r, 3)$=1, in the primitive cell of TBG, only A_1 is aligned with its counterpart A_2, while B_1, H_1 is aligned with H_2 and B_2 respectively. This situation is called the sublattice exchange odd (SE-odd).[50]

Basically, these two situations correspond to different geometric spatial stackings of two layers. However, it does affect something physically. Mele[50] found that the magnitude of the interlayer hopping potential displays different symmetries in two situations, sixfold-symmetric for (1) and threefold-symmetric for (2). Further investigation[51] revealed that there appears to be different states under two situations, a 'normal state' for (1) and a 'complementary state' for (2). The so-called complementary state can be accessed at small twist angles by adjusting the parameter related to the interlayer coupling theoretically.

2.2. Optical Properties Originating from Special Structure. Actually, TBG brings us a lot to investigate in optics field based on its inherent novel structure. TBG can be an excellent candidate for chirality investigation, which is mainly characterized by the circular dichroism (CD) effect. Chirality material is defined as a material that cannot be superimposed by its mirror image, and they are useful for circular polarizer,[52] chiral sensor[53] and spintronics.[54] CD is a crucial characterizer to detect the chirality of materials, which is often measured as ellipticity. Through stacking two CVD grown graphene layers together with precisely controlled twist angle, chiral TBG with left-hand and right-hand chirality was prepared successfully in the experiment by Kim *et al.*[55] [Fig. 4(a)]. The CD spectrometer was performed in TBG to obtain ellipticity. TBG displays an ellipticity up to 6.5 deg/μm across two layers, which is one of the highest compared with those chiral materials reported earlier.[56] The energy of CD peaks can be tuned by the twist angle. To reveal the origin of the large ellipticity in TBG, Matsuo and Gekko performed DFT calculation and showed that the large ellipticity is caused by

the interlayer optical transition. They found that a hybridized state delocalized across two layers is excited, where a helical current can be hosted, thus generating large ellipticity in TBG. Then, after the theoretical part of Ref. [56], Morell *et al.*[57] adopted a new method based on the continuum effective models and tight-binding theory to recalculate the chirality of TBG [Fig. 4(c)]. They found that the chirality of TBG can be estimated by calculating the Hall conductivity which vanishes when the twist angle approaches zero because the contribution from the highest-energy valence band to the second-lowest-energy conduction band cancels with that from the pair of bands with opposite energies. However, the contributions from each band do not cancel because of the relative rotation between two graphene layers. Therefore, a peak linked to the VHSs will still appear in the Hall conductivity spectrum (CD spectrum) [Fig. 4(b)]. These results proved it an efficient theoretical method to explore the chirality of TBG. After that, many theoretical studies have been carried out to obtain insight into possible factors that could change or modify the chiral properties of TBG. Stauber *et al.*[58] derived an effective (minimal) model to investigate the optical response of TBG in the terahertz wave region. They found that the CD spectrum of TBG can be enhanced by the doping as shown in Fig. 4(d). Moreover, Addison *et al.*[59] reported the effect of interlayer slip and twist angle on the chirality of TBG. Figure 4(e) shows the ellipticity as a function of the interlayer slip. As the slip increases, the ellipticity decreases at first and then increases. These studies revealed the vital roles that twist angle, doping, and interlayer slip are playing in determining the chiral properties of TBG. Moreover, as the layers of twisted graphene system increase, the chiral properties can also be programmed via varying multiple twist angles to achieve different chiral performance. However, the measuring device and sample preparation could still be a great obstacle for development of chiral two-dimensional materials.

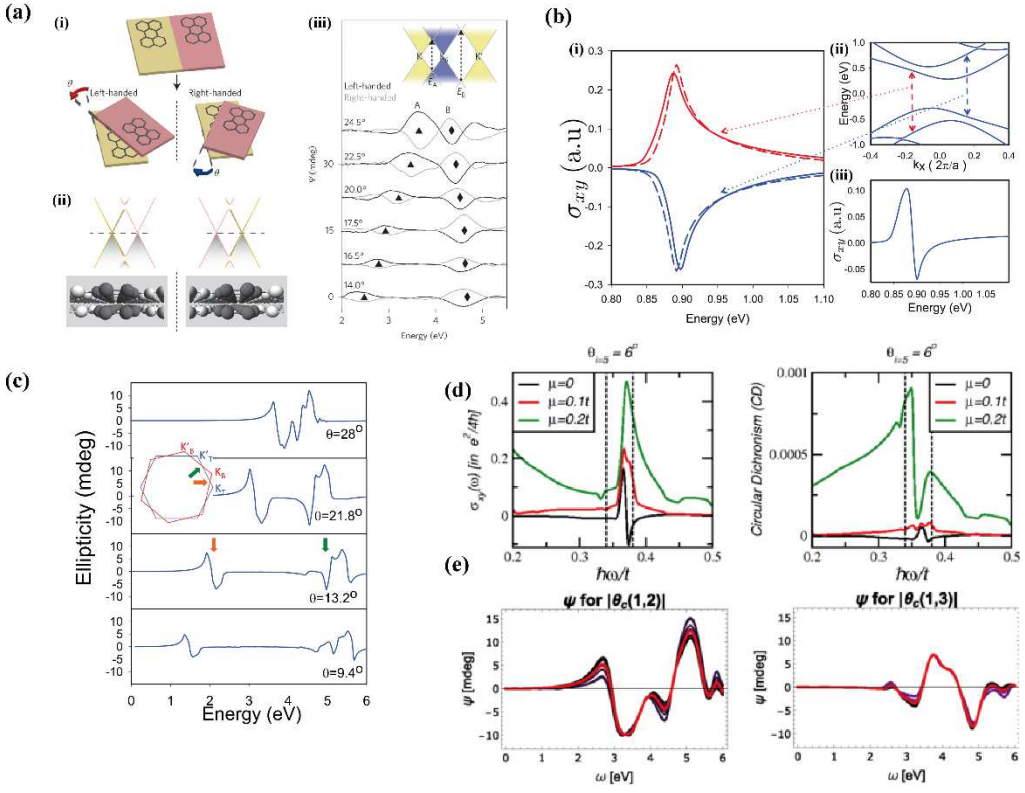

Fig. 4. (a) Schematic diagram of TBG preparation with right-hand and left-hand chirality. (ii) Electronic band of TBG. (iii) Circular dichroism spectra of left-hand and right-hand TBG with different twist angles (reproduced with permission from Ref. [55]). (b) (i) The Hall conductivity originated from two opposite transitions. The dashed line indicates that the Hall conductivity is zero when the twist angle is 0°. (ii) Electronic band structure of TBG, i.e., the interband transition process between the saddle points in the second highest valence band and the edge of the lowest conduction band (red dashed line). The blue dashed line indicates the opposite transition. (iii) Calculated total Hall conductivity of TBG with 5° twist angle. (c) Calculated ellipticity spectrum in TBG with 28°, 21.8°, 13.2°, and 9.4° twist angles. [(b), (c)] Reproduced with permission from Ref. [57]. (d) Calculated Hall conductivity and circular dichroism for different doping levels (reproduced with permission from Ref. [58]). (e) Circular dichroism as a function of frequency for $\theta_c(1,2)$ and $\theta_c(1,3)$ TBG. Different line in the picture correspond to the interlayer slip 0, 0 to 0.42, 0.24 (reproduced with permission from Ref. [59]).

In addition to the investigation of chirality of TBG, inversion symmetry breaking in TBG also provides new opportunity to observe the even-order harmonic generation. Yang *et al.*[60] demonstrated twist angle in hBN-capsulated TBG [Fig. 4(a)] offers a new approach to efficient second-harmonic generation. The second-order optical susceptibility is $\sim 2.8 \times 10^5\,\mathrm{pm}^2/\mathrm{V}$, and it is comparable to monolayer MoS_2 with well-known high optical nonlinearity.[61] Through choosing the incident wavelength ($\sim$1.58 eV), two-photon (3.16 eV) resonance could be turned on, the SHG intensity will be strongly enhanced [Fig. 4(b)]. The resonance energy can range from 0 to 4 eV, which is within widely studied spectrum windows. Apart from SHG, third-harmonic generation (THG) could also be resonantly enhanced and controlled by the twist angle. The intensity of THG is enhanced when the incident three-photon resonance coincides with the transition energy of VHSs, which makes it dependent on the interlayer twist angle.[62] Figure 5(c) shows the THG spectrum for different positions in the CVD TBG sample. When the voltage is 0 V, the THG intensity is 3.3–8.5 times stronger than that in SLG. It suggests that the THG intensity can be enhanced by the interlayer transition in TBG. When -1.8 V voltage is applied to the sample, the highest 60-times enhancement can be obtained in TBG [Fig. 4(d)]. The gate voltage can also contribute to the enhancement of THG. The results of these nonlinear properties justify the promising future of TBG in the nonlinear optics field.

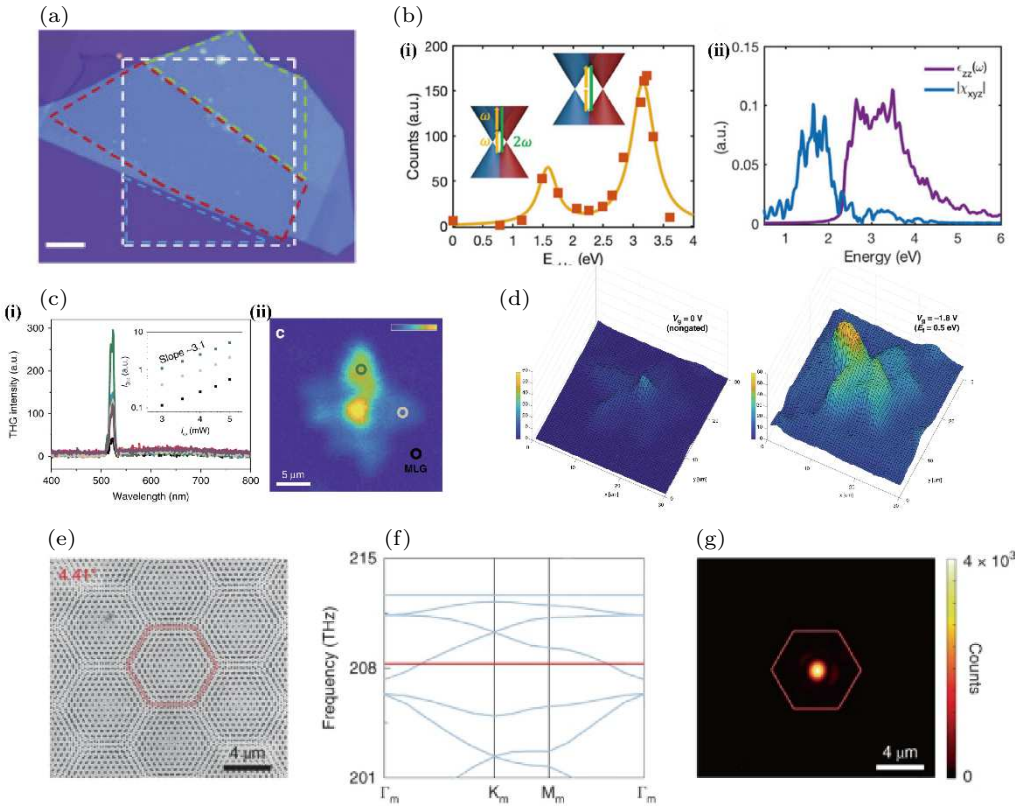

Fig. 5. (a) Optical image of hBN capsulated TBG with 8° twist angle. (b) (i) SHG signal as a function of transition energy between VHSs in TBG with different twist angles under 1.58 eV excitation energy. (ii) Imaginary part of linear permittivity along z direction, and the absolute values of χ_{xyz} in 21.8° TBG. [(a), (b)] Reproduced with permission from Ref. [60]. (c) (i) Spectrum of THG for MLG, and TBG with different twist angles. (ii) THG map of MLG, and TBG with different twist angles. (d) THG map of TBG at gate voltage $V_g = 0$ V, and $V_g = -1.8$ V. [(c), (d)] Reproduced with permission from Ref. [62]. (e) SEM image of OMTBG. (f) Calculated band structure of OMTBG with 4.41° twist angle. (g) Single-cell lasing patterns in OMTBG. [(e), (f)] Reproduced with permission from Ref. [63].

2.3. Momentum Space Model. As mentioned above, in TBG, once the top-layer graphene is rotated relatively to the bottom layer in real space, the moiré super cell will be formed under commensurate angles, which is much larger than the original graphene unit cell. Larger unit cell in real space corresponds to reduced moiré Brillouin zone (MBZ) in momentum space with reduced reciprocal vectors. The geometries of various 2D moiré systems were summarized in Ref. [64], which are instrumental for experimental observation of moiré patterns. In the TBG system, the MBZ is formed in the way as shown in Fig. 3(b). However, remember that the two inequivalent Dirac points of MBZ are from different layers this time. Con-

sequently, the coupling between states around these two Dirac points is directly related to the interlayer coupling in the real space.

By the way, the relative rotation between two Brillouin zones can induce novel phenomena in Raman spectra of TBG by introducing an additional rotational momentum vector (RMV). A new peak R′ with non-dispersive property is observed in Raman measurement by Lu *et al.*, intensity of which varies with twist angles, reaching a maximum at a certain angle.[65] The explanation for this novel peak can be such that when the electron is excited to produce an electron-hole pair, the electron will be elastically scattered by RMV and then be backscattered to the original momentum with the assistance of the phonon. Therefore, the relationship between RMV and twist angle determines that the larger twist angle will ask for higher excitation energy to observe this R′ peak. Therefore, RMV of TBG can characterize the phonon dispersion in TBG. Because both direction and magnitude of RMV are determined by the twist angle, these new Raman peaks' frequencies are directly related to twist angle, independent of excitation energy[66] [Fig. 6(c)]. These newly appearing Raman peaks, including those reported by Righi *et al.*,[67] the new D-like band and R peak found by Carozo *et al.*,[68] can be characteristic Raman bands to distinguish TBG from SLG [Fig. 6(a)].

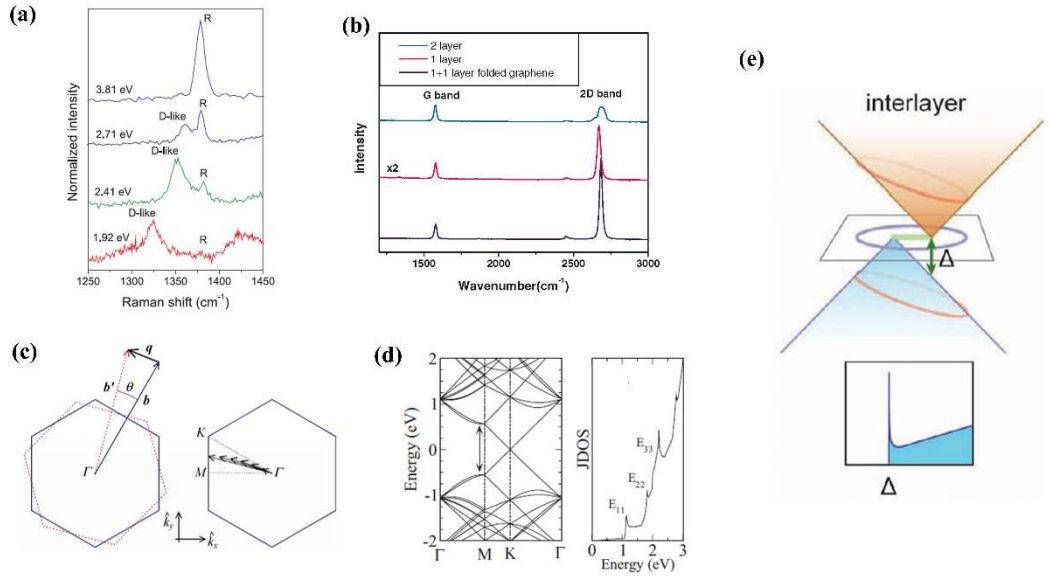

Fig. 6. (a) Raman spectra of TBG with twist angle 27° under four different excitation laser energies. New D-like band appears as excitation energy varies, all spectra have been normalized (reproduced with permission from Ref. [68]). (b) Comparison between different Raman spectra of SLG, bilayer graphene and TBG (reproduced with permission from Ref. [69]). (c) Determination of rotational momentum vector (left) and its evolution as twist angle varies from 0° to 30° (right) (reproduced with permission from Ref. [66]). (d) Electronic structure of TBG with twist angle around 11° (reproduced with permission from Ref. [70]). (e) Interlayer transitions between two Dirac cones, with the bottom figure showing the joint density of state (reproduced with permission from Ref. [71]).

Coming back to the model, theoretical analysis usually treats the twist as one layer's twist $\theta/2$ clockwise and the other layer's twist $\theta/2$ counterclockwise, which gives us a symmetric case to deal with [Fig. 3(b)]. After a detailed calculation of interlayer hopping in Ref. [41], the states from one layer are revealed only to couple with the nearest three states from the other layer based on the reasonable approximation that two-center hopping magnitude decays rapidly in momentum space. In momentum space, we take $K_{\mathrm{G}} = |\boldsymbol{K} - \boldsymbol{K}_\theta|$, then the vectors connecting two coupled states from two layers are $\boldsymbol{q}_1 = K_{\mathrm{G}}\,(0,-1)$, $\boldsymbol{q}_{2,3} = K_{\mathrm{G}}\left(\pm\sqrt{3}/2, 1/2\right)$, which are $q_{\mathrm{b}}, q_{\mathrm{tr}}, q_{\mathrm{tl}}$ in Fig. 3(c), respectively. Assume that a state residing on $\boldsymbol{p}_1$ around $\boldsymbol{K}_{\theta/2}$ (thus from layer 1) couples with the state on $\boldsymbol{p}_2$ around $\boldsymbol{K}_{-\theta/2}$ (from layer 2), then the interlayer hopping term should be

$$T^{\sigma,\xi}_{\boldsymbol{K}_{\theta/2}+\boldsymbol{p}_1,\boldsymbol{K}_{-\theta/2}+\boldsymbol{p}_2} = T_{\boldsymbol{q}_{\mathrm{b}}}\delta_{\boldsymbol{p}_2-\boldsymbol{p}_1,\boldsymbol{q}_{\mathrm{b}}} + T_{\boldsymbol{q}_{\mathrm{tr}}}\delta_{\boldsymbol{p}_2-\boldsymbol{p}_1,\boldsymbol{q}_{\mathrm{tr}}} + T_{\boldsymbol{q}_{\mathrm{tl}}}\delta_{\boldsymbol{p}_2-\boldsymbol{p}_1,\boldsymbol{q}_{\mathrm{tl}}}, \tag{8}$$

where σ, ξ label different sublattices from two layers, respectively. $T_{\boldsymbol{l}}$, holding a different form for different $\boldsymbol{l}$, is in matrix notation which contains four interlayer intersublattice coupling conditions:

$$T_{\boldsymbol{l}} = \begin{pmatrix} T_l^{\mathrm{AA}} & T_l^{\mathrm{AB}} \\ T_l^{\mathrm{BA}} & T_l^{\mathrm{BB}} \end{pmatrix}. \tag{9}$$

Then the Hamiltonian for TBG can be divided into intralayer and interlayer terms:

$$H = H_{\mathrm{SLG}}\left[R\left(-\frac{\theta}{2}\right)\boldsymbol{k}\right] + H_{\mathrm{SLG}}\left[R\left(\frac{\theta}{2}\right)\boldsymbol{k}\right] + H_{\mathrm{inter}}, \tag{10}$$

where

$$R(\theta) = \begin{pmatrix} \cos\theta & -\sin\theta \\ \sin\theta & \cos\theta \end{pmatrix} \tag{11}$$

acts on $\boldsymbol{k} = (k_x, k_y)^{\mathrm{T}}$ and exerts clockwise and counterclockwise rotation on two intralayer Hamiltonians, respectively, for symmetric simplification. What is intriguing is the interlayer term, which leads to the extension of "shells" in momentum space. Within the MBZ, state from layer 1 residing on $\boldsymbol{k} = (k_x, k_y)$ couples with states from layer 2 on other three k points $\boldsymbol{k}+\boldsymbol{q}_{1,2,3}$ [the first shell as shown as purple dashed zone in Fig. 3(c)]. Also, these three states couple with other states from layer 1 through the vectors $-\boldsymbol{q}_i (i = 1, 2, 3)$ (the second shell). Thus, the enlargement of basis to describe the Hamiltonian of TBG system can be continued shell by shell, which brings up to infinite dimensions of total Hamiltonian. In actual calculations, we should add cut-off on the Hamiltonian to make numerical solution accessible. Essentially, the energy dispersion in the low-energy range will be more accurate if we construct a large enough Hamiltonian. Due to the large number of atoms in the supercell of TBG, the DFT method could be time-consuming and less efficient. Hence, the main method to resolve basic band structure of TBG is the continuum model,[21,41,44,72] along with DFT[73,74] calculating some coupling parameters.

3. Atomic Reconstruction. Although theoretical analysis gives us a clear picture of TBG, a realistic situation can be very sophisticated when considering corrugation and ripple in the sample. Uchida *et al.* found that the twist will induce additional corrugation within the sample, resulting in the distinct interlayer distances at different stacking areas. Generally, the interlayer distance becomes the largest at the AA-stacking regions, the smallest at the AB-stacking regions [Fig. 3(d)]. This variation does not rely on the detailed atomic structure but on the whole moiré pattern. Meanwhile, a critical angle exists where the corrugation becomes prominent.[48] Recently, local strain of bilayer graphene can be detected with high sensitivity through the method developed by Du *et al.*[75] They overcame the obstacles of rare infrared response of bilayer graphene by applying a vertical electrical field, which breaks the symmetry of two layers and introduces a finite electrical dipole moment. Consequently, the activated phonon can then participate in electronic transitions, generating a strong Fano resonance. This method paves the way to probe local strains in non-polar crystals and enables people to investigate strain-induced phenomena.

Besides the effect of corrugation, another effect, which results in the deformation of original moiré superlattice, attracts more interest. After the formation of the moiré superlattice, three alternating stacking configurations appear (AA-, AB- and BA-stacking orders) within a supercell as shown in Fig. 3(e). However, at small twist angles, the drastically increased area of energetically unfavorable AA-stacked regions in TBG will spontaneously induce the relaxation of moiré superlattice, which is often referred to as "atomic reconstruction" [Fig. 3(f)]. Yoo *et al.* pointed out that formation of commensurate domains via reconstruction in TBG often takes place at small twist angles, comprising triangular domains separated by sharp mirror boundaries which indicates an interfacial atomic reconstruction in TBG. As the twist angle increases, the triangular domain contrast turns into one-directional fringes, which often happens for moiré structures without reconstruction, implying that the reconstruction strength increases with decreasing twist angle. The reconstruction of the moiré pattern will apparently alter the electronic structure of TBG, changing the behavior of conductance measurement and density of states (DOS). They also found that the unreconstructed TBG usually presents multiple sharp features in DOS spectra, which are unstable when the twist angle varies slightly. This means that tiny changes in the twist angle should be taken into account in measurement of low-energy transport. However, for reconstructed TBG, it shows several main sharp features in the DOS spectra, arising from Dirac-like band crossings exhibited in the reconstructed electronic spectrum, indicating the emergence of the "secondary Dirac spectrum". The main results are shown in Fig. 7(a). They also compared the dependence of resistance in different systems including Bernal-stacked bilayer graphene and TBG of large (2.8°) and small (0.46°) twist angle and found that they exhibit distinct properties. The Bernal-stacked bilayer graphene's resistance will increase with increasing displacement because of the gap-opening property; the large-twist TBG's resistance will decrease with the increasing displacement because of its less resistive property due to the opposite doping of two layers. The small-twist TBG will show a more complicated pattern owing to the formation of a network of 1D topological channels along the domain boundaries which are closely related to the locally varying pseudo-magnetic field induced by lattice strain.[33]

The significance of interlayer stacking configurations of TBG also endows atomic reconstruction with a crucial role in the external measurement of some physical quantities like tip-TBG conductivity in the experiment by Zhang *et al.* This kind of conductivity was measured by applying bias voltage between the tip and the bottom layer of TBG and then measuring the current as the tip sweeping the surface of TBG sample, which is found to increase when the twist angle decreases, while it begins to decrease notably after reaching a critical angle about 5° [Fig. 7(b)].[49] Actually, this abnormality appears in the regime where atomic

reconstruction is observed. To find out whether or not the deformation of moiré superlattice results in this anomaly, authors revealed in theoretical calculations that the regions showing relatively low and high conductivity correspond to AB-/BA- and AA-stacked regions, respectively. Based on atomic reconstruction results, when twist angle reaches a small enough value, spontaneous relaxation will increase the proportion of AB-/BA-stacked regions and reduce that of AA-stacked regions within the moiré unit cell. This reconstruction will, however, weaken the averaged current signals. For unexpected nonmonotonic behavior of tip-TBG conductivity at small twist angles, the authors believe that it is highly related to local carrier density based on the fact that local density of states also reduces with decreasing twist angles. In further calculations, Zhang *et al.* found that the variation of local carrier density on the top graphene surface mainly originates from AA-stacked regions where the overlap of interlayer electron states is weaker than that in AB-stacked regions. This characteristic makes the electrons in AA-stacked regions act more like carriers instead of bonding electrons, which contributes to local carrier density.[49] Then, when atomic reconstruction takes place, the local carrier density will decrease along with diminishing AA-stacked regions accordingly. In a word, atomic reconstruction plays a pivotal role in measurements of tip-TBG conductivity at small twist angles.

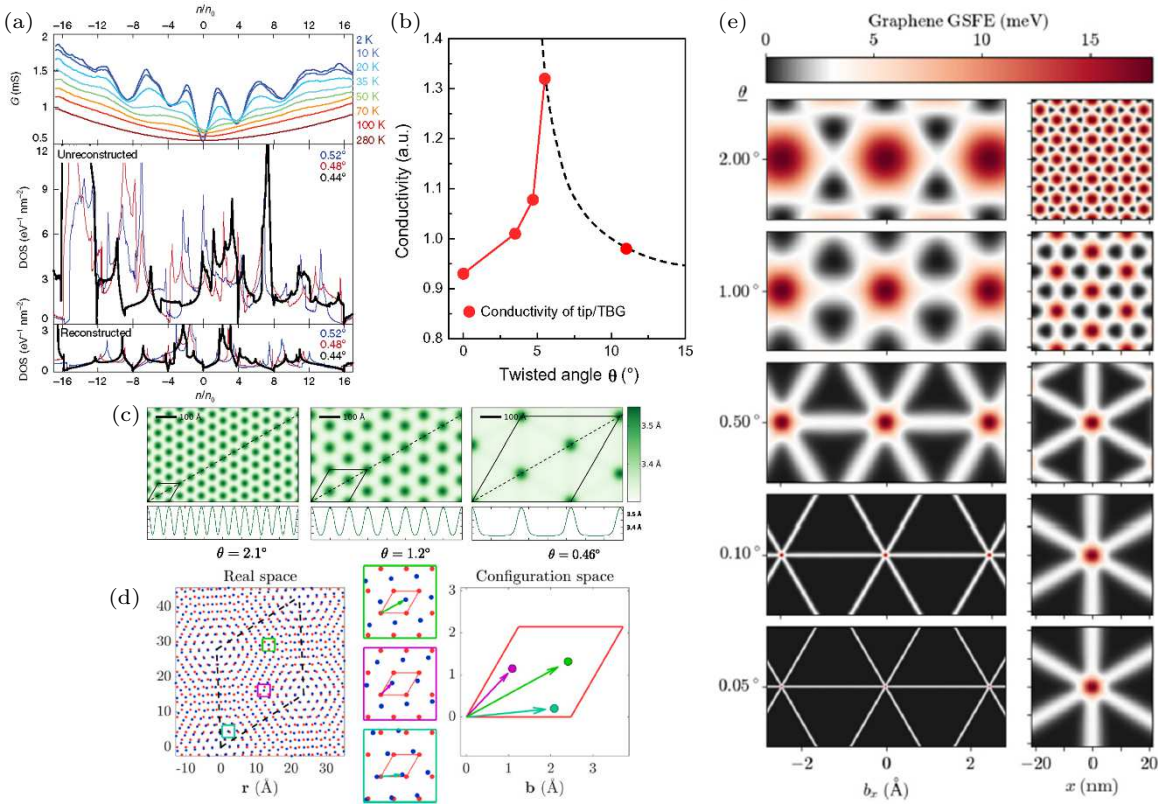

Fig. 7. (a) Conductance measurement as a function of carrier density under different temperatures (upper). Theoretical DOS results with three different twist angles for unreconstructed and reconstructed situations (lower) (reproduced with permission from Ref. [33]). (b) Abnormal decrease of tip-TBG conductance after reaching a critical angle near 5° (reproduced with permission from Ref. [49]). (c) Out-of-plane distance when atoms are allowed to move towards any directions (reproduced with permission from Ref. [76]). (d) Relationship between real space and configuration space. (e) Generalized stacking fault energy (GSFE) of TBG in configuration space and real space. [(d), (e)] Reproduced with permission from Ref. [77].

The existence of this important reconstruction of the geometrical moiré pattern at small twist angles is investigated in many theoretical works. Van Wijk *et al.* did molecular simulation and found that this reconstruction, however, cannot be appropriately expressed into a sinusoidal-like function. In their article, so-called "hot-spot" regions divided by flat domains are formed with considerable out-of-plane displacements. It was found that when only atomic displacement along x and y dimensions is allowed, the area of AA-stacked regions decreases while that of AB-stacked regions increases after relaxation. As the twist angle decreases, the deformation of the bond varies from sinusoidal-like to localized contraction close to the AA areas. When the atom is allowed to move along the z dimension, the z direction will become

the main direction which atoms move towards. For the whole simulation area, the out-of-plane distance also varies spatially and also exhibits localized property when it approaches the small angle [Fig. 7(c)]. By using the STM method, out-of-plane deformation will be accessible at the so-called hot-spot regions. Similar to the results of Yoo *et al.*, the deformation is able to induce the modification of the pseudo-electrostatic potential, which is dependent on local uniform compression and a (pseudo)-vector potential.[76]

After that, Carr *et al.* developed another method to describe the relaxation problem, the central topic of which is "minimizing total energy over a collection of all possible local atomic environments". They divided the total energy into two parts: intralayer and interlayer energy, then described the relaxation as a function of a position-dependent displacement vector field. The intralayer and interlayer coupling parameters can be obtained from DFT software (*ab initio* calculation). Since the atomic reconstruction is highly related to the interlayer coupling, they mainly focused on the investigation of the interlayer energy term. The interlayer energy per moiré unit cell can be well described by generalized stacking fault energy (GSFE), which only depends on the local stacking configuration. The relaxation will result in the distortion of layers to maximize the area of lowest-energy stacking order and to minimize the area of highest-energy stacking order. Specifically, at small interlayer misalignment, uniform stacking orders are obtainable with only a little lattice straining, while the increase of misalignment will demand more strain, which makes the formation of uniform domains more unrealizable. They also mapped the atoms in real space to the configuration space with the aim of treating stacking orders more neatly [Fig. 7(d)]. The most charming characteristic of this configuration space is that the atomic displacement in this space is periodic even for the incommensurate structure. They found expansion of lowest-energy stacking regions and reduction of higher-energy stacking regions in configuration space, both of which results from the relaxation. Then, thin lines and nodes will emerge in the configuration space. Consequently, atomic reconstruction will take place in real space, forming similar lines and nodes[77] [Fig. 7(e)].

About this important parameter (GSFE) in theoretical calculation, Zhou *et al.* investigated different methods to calculate it for different stacking systems including graphene/graphene, hBN/hBN, graphene/hBN systems. There are several methods to calculate the GSFE, they are DFT-D2 (DFT dispersion correction), vdW-DF2 (van der Waals density functionals), MGGA-MS2 (meta-generalized gradient approximation) and ACFDT-RPA (adiabatic-connection fluctuation-dissipation theorem within the random phase approximation). Among these methods, ACFDT-RPA gives the most accurate and general results, but costs the most resources. They also provided the solution for reducing calculation time of the ACFDT-RPA method. They found that the curves of interlayer separation after relaxation resembles those of GSFE curves for different stacking systems. The interlayer spacing and the GSFE can both be expressed by the same functional, but for systems with different symmetries, different independent parameters can be used. GSFE results for different stacking systems can be referred to in detail in Ref. [78].

Besides the molecular simulation and the calculation of GSFE via *ab initio* methods, there is another way developed by Nam and Koshino to describe the spontaneous relaxation of TBG, which deems two layers of graphene as two coupled chains. Similarly, the model also includes two types of energy, the intralayer interatomic elastic energy and the interlayer binding energy. The main method to get the relaxed structure is to minimize the total energy by solving the Euler–Lagrange equations. The researchers pointed out that there is an important parameter to describe the harmonics which participates in the chain vibration (layer displacement), which directly leads to different deformations. It is found that the reconstructed structure will affect the electronic structure prominently at small twist angles ($<2^\circ$) and in both relaxed and non-relaxed structures, the vanishing of the Fermi velocity will appear but the relaxed one will make the critical angle smaller. In a relaxed structure, the Fermi velocity is relatively larger than that in non-relaxed one. The lattice relaxation will both affect the interlayer Hamiltonian and intralayer Hamiltonian.[79]

Besides all these experimental and theoretical results about atomic reconstruction, there are other experiments including the localization of lattice observed by the nano-Raman spectroscope,[80] conversion between the unreconstructed and reconstructed structure via the STM-tip[81] and reconstructions in other twisted TMD materials.[82]

4. Observation of Moiré Supercell. To deepen the understanding of the twisted graphene system, in previous research, researchers used a variety of experimental methods to observe moiré patterns.

4.1. Electron Microscope Method. A most common method is to use a transmission electron microscope (TEM). Figure 8(a) shows typical bright field high-resolution TEM (HR-TEM) images of misorientation-caused moiré patterns.[65] As the twist angle gradually increases, the period of the moiré pattern gradually decrease, which is consistent with formula (7). The inset shows the selected area electron diffraction image of the TEM illuminated area. With the angle between the diffraction crystal axes, the torsion angle can be accurately measured.

In addition to the TEM bright-field images, in experiments, TEM dark-field images can also be used to characterize the lattice reconstruction in the moiré superlattice. The dark-field TEM image formed by diffracted electrons is very sensitive to the incompleteness and orientation of the lattice. In the experiment, the distribution of the AB/BA domain in the moiré lattice can be clearly distinguished in dark-field TEM image. Figure 8(b) shows the schematic diagrams of TBG before and after the atomic reconstruction (as AB and BA regions are energetically favorable stacking and AA region is an unfavorable stacking). Figure 8(c) shows a dark field high-resolution TEM (HR-TEM) images of twisted graphene.[33] The periodic array of AB/BA domain structures is separated by mirror boundaries. As the twist angle increases, the strength of lattice reconstruction gradually weakens just as mentioned above. This is manifested as a decrease in the contrast of the AB/BA triangle domains, which gradually degenerates to one-directional fringes.

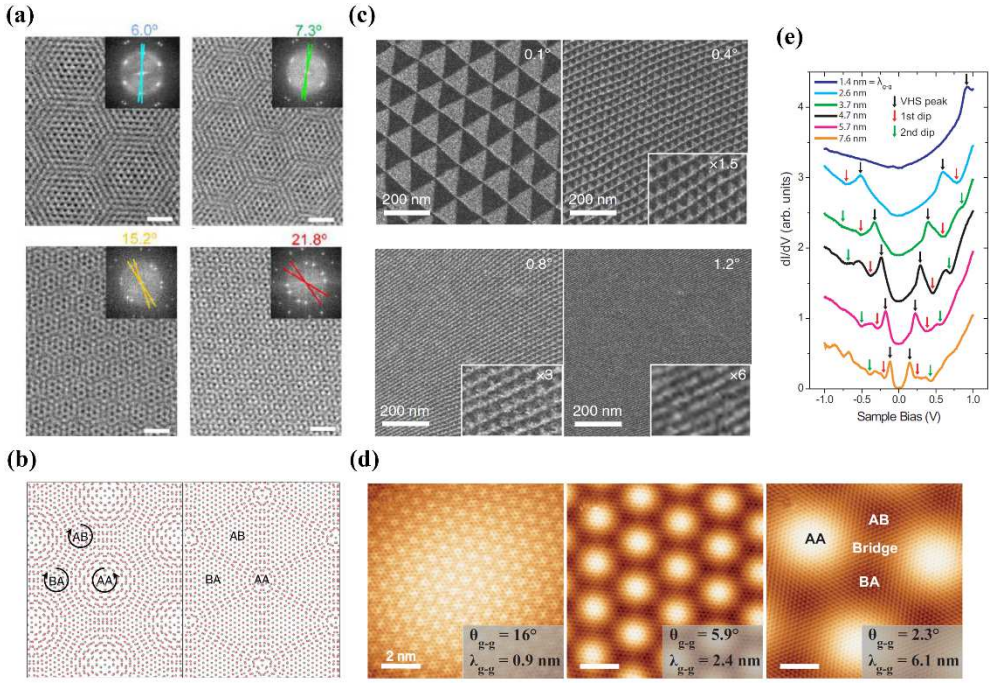

Fig. 8. (a) The HR-TEM images of BLG in different twist angles. Fast Fourier transform (FFT) patterns are inserted to present the twist angles. All the scale bars are 1 nm (reproduced with permission from Ref. [65]). (b) Scheme of twist graphene superlattice, before (left) and after (right) atomic reconstruction. (c) TEM dark-field images of twisted graphene with different angles. [(b), (c)] Reproduced with permission from Ref. [33]. (d) STM images of Moiré pattern for different graphene-graphene twist angles. (e) STS spectrum of twist graphene with different twist angles. The STM dI/dV spectrum shows three characteristic peaks (marked by arrow). [(d), (e)] Reproduced with permission from Ref. [83].

4.2. Scanning Probe Microscopy Method. Scanning probe microscopy (SPM) is also widely used in the detection of moiré patterns. A scanning tunneling microscope (STM) is the first SPM that came out, and it is commonly used in the characterization of moiré fringes. STM differential conductance spectroscopy is usually employed to study the local density of states (LDOS) and the energy level structure of the quasi-two-position electron gas on the surface of materials.

According to the quantum tunneling theory, the tunneling current between the STM tip and the sample surface satisfies:[84]

$$I = \frac{4\pi e}{\hbar}\int_0^{eV} \rho_{\rm s}(E_{\rm F} - eV + E)\rho_{\rm t}\left(E_{\rm F} + E\right)|M|^2\, dE, \tag{12}$$

where $\rho_{\rm s}$ and $\rho_{\rm t}$ are the LDOS of the sample surface and the tip, respectively, and M is the tunneling matrix element. It can be considered that $\rho_{\rm t}$ does not change significantly during the test, then formula (12) can be transformed to

$$\frac{dI}{dV} \propto \rho_{\rm s}(r_0, E), \tag{13}$$

which indicates that the tunneling current dI/dV is directly related to the spatial distribution of LDOS on the sample surface.

For the twisted graphene system, due to lattice reconstruction and interlayer coupling, the surface local electron density of states (LDOS) and the interlayer valence electron density of AA and AB domains show great differences,[49] which is directly reflected in their surface conductivity and tunneling current intensity. Figure 8(d) shows the STM images of the twisted graphene with different angles. Lattice reconstruction between AA and AB domains is significant, that is,

the LDOS of the AA stacking regions is much larger than that in AB stacking regions.

In addition, the scanning tunnel spectrum (STS) can also characterize the Van Hove peak formed by the overlap of the Dirac cones.[83] Figure 8(e) presents the STS spectrum of twist graphene with different twist angles. Near the zero-bias voltage, the STS spectrum of the twisted graphene has obvious characteristic peaks. The peaks on the curve correspond to the van Hove peaks at different energies, that is, the position of the saddle point in the twisted system energy band structure.

Except the common detection methods such as TEM and STM, there are some more special methods used to detect the moiré periodic structure. Conductive probe atomic force microscope (C-AFM) is often used to study the electrical conductivity of samples and high-resolution imaging electrical characteristics. During the detection process, the conductive tip is in contact with the sample to apply a bias voltage. The current between the two is measured when the probe raster scans the entire surface to form a local conductivity or current graph.

The local atomic reconstruction of twisted graphene has a strong control on the electrons in the system. This regulation is not only reflected in the local density of electrons, but also in the local average carrier concentration and the vertical conductivity between layers. In 2019, Zhang *et al.*[49] first applied C-AFM to observe the regulation of the surface carrier concentration and vertical conductivity of the twisted system by the moiré periodic structure.

Figure 9(a) shows a schematic diagram of C-AFM for measuring the vertical conductivity of double-layer graphene on h-BN substrate (there are angle differences in these twisted regions). Figure 9(b) shows the C-AFM current image measured on bilayer graphene with different twist angles (1.1°, 3.0°, and >12°). When bias is applied on the surface of twisted graphene, the AA stacking area with higher valence electron concentration and LDOS will exhibit higher carrier concentration and obtain a larger current signal under the same bias voltage. Figure 9(c) shows the periodic current profiles across the AA/AB domains with different twisted angles. Figures 9(d)–9(e) show a typical current distribution obtained by scanning the surface of a TBG using CAFM, with twist angles of 2.9° and 0.6°, respectively. Among them, the AA domain is marked with a black circle. There is a significant difference in the proportion of AA and AB domains in different angles, which stems from the variation in angles and the lattice reconstruction occurring in low-twisted angles system. This divergence in the proportion of area also leads to the difference in the macroscopic conductivity of the graphene with different twist angles.

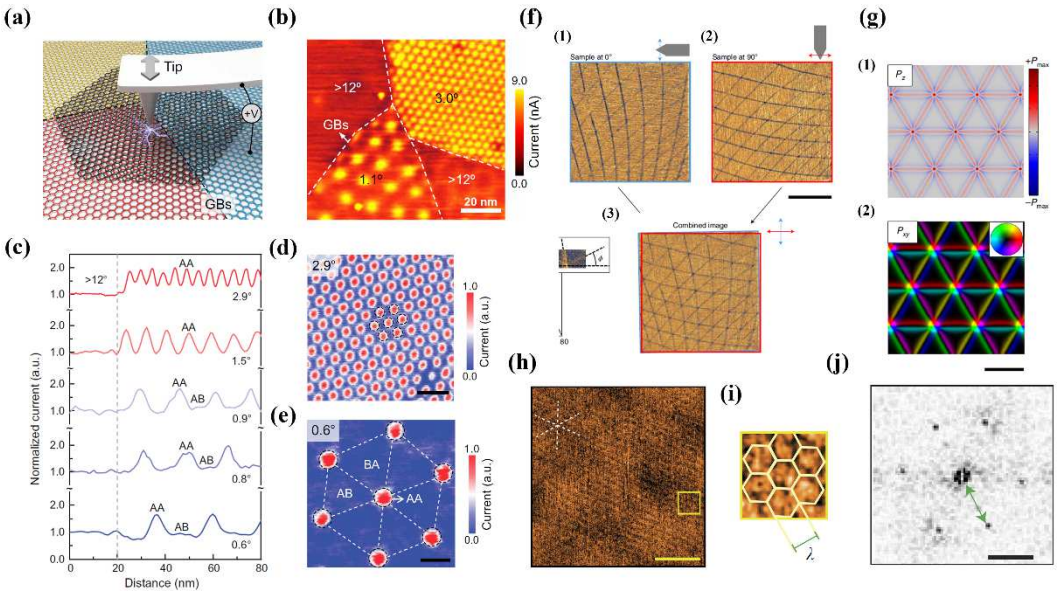

Fig. 9. (a) Schematic diagram of C-AFM for measuring the vertical conductivity of double-layer graphene. (b) C-AFM current image measured on bilayer graphene with different twist angles (1.1°, 3.0°, and >12°). (c) Periodic current profiles across the AA/AB domains in different twisted angles. [(d), (e)] Current distribution obtained by scanning the surface of a TBG using CAFM, with twist angles of 2.9° and 0.6°, respectively. (a)–(e) Reproduced with permission from Ref. [49]. (f) Vector PFM image performed by a sample rotation of ∼90°. The PFM phase images at 0° (1) and 90° (2) can be recombined to reconstruct the full moiré pattern image (3). (g) Out-of-plane polarization P_z localized at the highest strain-gradient regions (1), and in-plane polarizations P_{xy} (2). [(f), (g)] Reproduced with permission from Ref. [85]. (h) Partial AFM image of twisted graphene. (i) Close-up of the yellow square in (h). (j) Fourier transform of the lattice of (h). (h)–(j) Reproduced with permission from Ref. [86].

Like C-AFM, the piezoelectric force microscope (PFM) also detects the electrical properties of the sample surface by applying a voltage to the tip of the needle. During the imaging process of PFM, the amplitude and phase response of the cantilever beam after the voltage is applied are recorded. Among them, the phase map in the PFM provides information about the direction of electrical polarization relative to the electric field, and the amplitude map shows the magnitude of the piezoelectric response. This signal can usually be used to identify the location of the domain wall. In 2020, McGilly *et al.*[85] reported using the PFM to characterize the lattice periodic structure of twisted graphene.

When the stacking of the moiré superlattice changes from AB to AA and saddle points, the symmetry is broken, and formulate a large strain gradient. The local strain gradient will cause flexoelectric effects and local polarization. Here, the correlation between strain gradient and electric polarization can be expressed by

$$P_\alpha = \mu_{\alpha\beta\gamma\lambda}\frac{\partial \varepsilon_{\gamma\lambda}}{\partial x_\beta}, \tag{14}$$

where P_α is the electric polarization, $\mu_{\alpha\beta\gamma\lambda}$ is the coefficient, and $\frac{\partial \varepsilon_{\gamma\lambda}}{\partial x_\beta}$ is the strain gradient. That is, although the AB domains with the largest proportion of torsion graphene have no significant flexoelectric effect, there is a strong flexoelectric effect in the AA domain and the domain wall. This strain-induced regional polarization is detected by the PFM tip. Figure 9(f) shows vector PFM image performed by a sample rotation of ∼90°. The PFM phase images at 0° (1) and 90° (2) can be recombined to reconstruct the full moiré pattern image (3). The calculation results of flexoelectric coupling [Fig. 9(g)(1)] gives rise to out-of-plane polarization P_z localized at the highest strain-gradient regions; that is, AA sites and domain walls. However, the in-plane polarizations P_{xy} [Fig. 9(g)(2)] appear in the vicinity of the domain walls, which have polar vectors of opposite direction and vortices surrounding the AA sites.

What is more, friction atom force microscopy (friction AFM) has also been utilized to resolve large period moiré superlattices.[86] As shown in Fig. 9(h), Schmidt *et al.* drew a partial AFM image of twisted graphene, where the white dash indicates symmetry directions of the superlattice. Figure 9(i) shows the close-up of the yellow square in Fig. 9(h). Figure 9(j) shows Fourier transform of the lattice of Fig. 9(h).

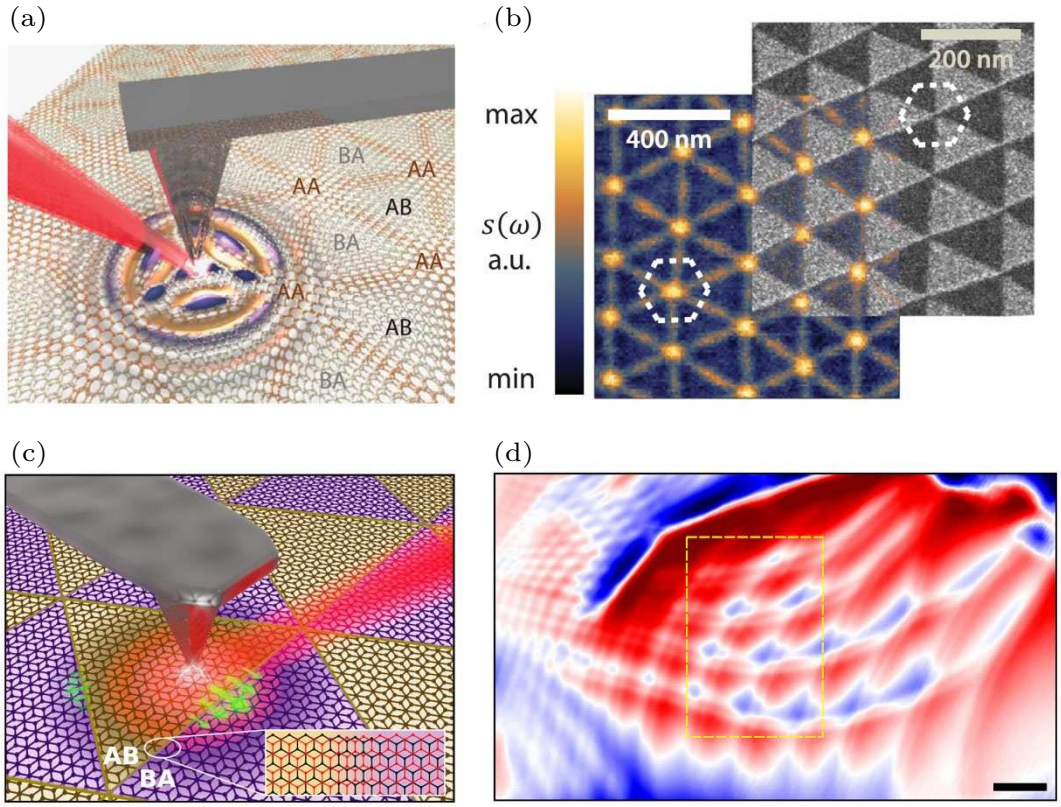

Fig. 10. (a) The scheme of infrared (IR) nano-imaging experimental setup. (b) Visualizing of the nano-light photonic crystal formed by the soliton lattice (left), and the dark-field TEM image of a TBG sample (right). [(a), (b)] Reproduced with permission from Ref. [87]. (c) Schematic illustration of near-field photocurrent experiments. (d) Local photo-thermoelectric effect induced by the fine structure of the moiré superlattice. [(c), (d)] Reproduced with permission from Ref. [88].

In recent research, near-field optics technology has begun to be used to resolve the plasmon polaritons and local photoelectric properties inside the moiré superlattice. In 2018, Sunku *et al.*[87] reported the research on optical conductivity distribution and plasmon propagation in the moiré superlattices by using infrared (IR) nano-imaging experimental setup. The scheme of this testing system is shown in Fig. 10(a). Through the near-field optical excitation achieved by the tip, researchers observed the nano-light photonic crystal formed by the soliton lattice [Fig. 10(b)]. Comparing the light conductivity distribution map (left) with the dark-field TEM image (right), an enhancement of local optical conductivity at solitons can be seen between AB and BA triangular domains.

Similar methods are also used to characterize the near-field photocurrent changes caused by the moiré periodic structure. In 2021, Hesp *et al.* realized the visualization of the photoelectric response inside the Moore lattice by means of near-field optics.[88] Figure 10(c) shows the schematic illustration of near-field photocurrent experiments. Figure 10(d) shows the local photo-thermoelectric effect induced by the fine structure of the moiré superlattice.

4.3. Comparison of Different Methods. As a summary, we compared the moiré pattern characterization methods mentioned above in terms of versatility, resolution, test sample preparation complexity, and object scalability (Table 1). The local density of states and electronic structure are very important for studying the twisted superlattice system. In this regard, the STM and STS methods occupy the top position. The STM images can obtain an intuitive surface electronic density distribution, and the STS test mode can accurately determine the position of the saddle point in the electronic structure of the rotation angle. Especially in condensed matter physics experiments related to the twisted system, STM/STS is almost indispensable. In terms of the resolution and scalability of the moiré pattern, the electron microscopy method (TEM) has advantages that other cannot match. Its spatial resolution can reach nanometer level, and the influence of torsion angle is ignored. The test object contains almost all kinds of two-dimensional materials. However, for both STM/STS and TEM, the target sample needs to be transferred to a special substrate (STM/STS usually needs to transfer the sample to the surface of the gold film, and TEM needs to use a special copper mesh or silicon nitride microgrid).

For research of the twisted system, whether the test method can be extended to other two-dimensional material systems is very important. In this respect, both TEM and PFM have outstanding performance, and are suitable for research of various systems including twisted graphene, TMDS materials, boron nitride, and so on. In general, STM/STS and TEM are the most used means to characterize moiré patterns. The second is PFM, which has good prospects in research of various twisted systems. C-AFM, friction AFM, infrared (IR) nano-imaging and near-field photocurrent also have their own application areas.

Table 1. Comparison of different methods.

Method	Versatility	Resolution	Preparation complexity	Experimental scalability
STM/STS	Good	Inferior	Excellent	Good
TEM	Good	Good	Excellent	Good
C-AFM	Excellent	Good	Good	Good
PFM	Average	Average	Average	Excellent
Friction-AFM	Inferior	Poor	Inferior	Inferior
Infrared (IR) nano-imaging	Good	Excellent	Good	Excellent
Near-field photocurrent	Excellent	Good	Excellent	Excellent

5. Unique Electronic Properties of TBG—5.1. Interlayer Coupling. Interlayer coupling of TBG is an important parameter not only in theoretical calculation but also in experimental measurements. In TBG, complicated behavior could show up due to alternating stacking orders in the structure, which makes the twist angle influence the interlayer coupling, specifically, interlayer resistivity/conductance prominently. AB-stacked bilayer's interlayer conductance can be 4 times larger than that of 30°-TBG, which demonstrates the difference between coupled and decoupled situation.[89] In 2013, Kim *et al.* focused on the interlayer coupling and found that interlayer resistivity of TBG, which is inversely proportional to the temperature, is several orders larger than intralayer resistivity [Fig. 11(a)]. The temperature dependence of interlayer resistivity can be attributed to phonon-assisted tunneling,[90] where higher temperatures provide phonons with larger momentum to compensate for the mismatch of two Fermi surfaces (FS). Consequently, when the twist angle is fixed, higher temperature leads to overlap of FSs of valleys from two layers, enhancing the interlayer conductance.[91] Likewise, under room temperature, smaller twist angle makes the phonon-mediated transport easier because of smaller momentum mismatch of FSs. This model also applies to relatively twisted graphite bulks.[92]

Generally, researchers are more interested in the

small twist angle regime, but actually, large twist angles can also lead to attractive results, too. Among these largely TBG, 30° TBG receives much more attention because it is situated at the symmetry boundary in the twist angle regime, which could cause many bizarre properties. Yao *et al.* discovered the existence of mirror Dirac cones in 30° quasi-crystalline TBG [Fig. 11(b)]. And a gap opening is observed between the original and the mirror Dirac cones.[46] Similar observations along with theoretical calculations are also reported by Ahn *et al.*, where the 12-fold symmetric pattern and significance of high-order Umklapp scattering are revealed.[93] These additional Dirac cones originate from generalized Umklapp scattering mediated by graphene's reciprocal vectors, which is governed by the selection rule in Refs. [93,94]. To describe the electronic properties of 30° quasi-crystalline TBG, Moon *et al.* established a simple model where 12-fold resonant states of Dirac fermions are appropriately captured, the wavefunction of which features the dodecagonal quasicrystal tiling pattern.[94] They characterized the sensibility of the system to tiny change of twist angles by showing the properties of 29.84° TBG. They also reinforced the convincement of their model by comparing it with the results based on finite-size tight-binding model, where they found the localized states. Actually, the "quasicrystalline bands" can be modified by adjusting interlayer coupling strength such as applying external pressure and electric field. These factors were well depicted by Yu *et al.*[95] They found that 12-fold resonant states can be pushed towards Fermi level as the pressure increases, which could be the precursor of possible emergence of correlated phases.

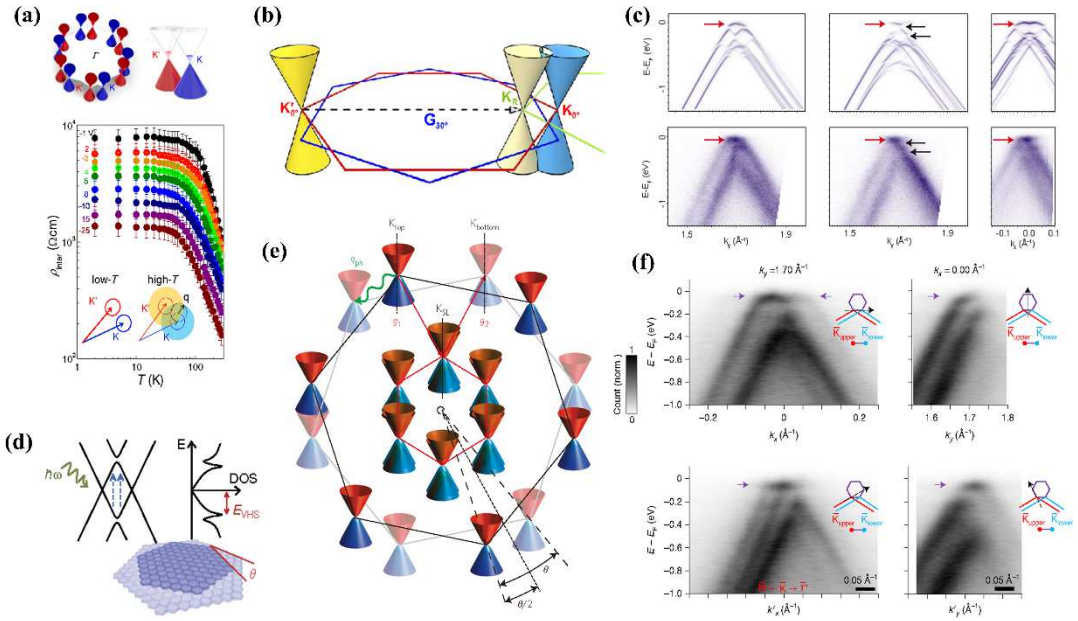

Fig. 11. (a) Momentum mismatch between two Dirac cones from different layers (upper) and temperature dependence of interlayer resistivity (reproduced with permission from Ref. [91]). (b) The formation of mirror Dirac cone arising from the scattering process of Dirac cone of one layer assisted by the reciprocal vector of the other layer (reproduced with permission from Ref. [46]). (c) Nano angle resolved photoemission (Nano ARPES) result of TBG along different cuts in momentum space. The flat bands are marked by red arrows and black arrows mark the appearance of hybridized gap (reproduced with permission from Ref. [34]). (d) Schematic diagram of optical transition between two van Hove singularities (VHSs) when incident photon matches the energy separation between VHSs (reproduced with permission from Ref. [96]). (e) Reduced Brillouin zone for twist angle $\theta = 21.8°$ and $38.2°$ (reproduced with permission from Ref. [97]). (f) ARPES result of TBG near the magic angle. Different pictures are taken along different paths in momentum space as shown in the insets. Purple arrows label the existence of flat bands (reproduced with permission from Ref. [98]).

In addition, merge and gap-opening in DOS spectrum were well characterized. Applying electric field will result in energy splitting between states from different layers, which will destroy the 12-fold symmetries of hybridized states. However, external pressure can reduce the on-site energy difference between layers, thus slightly recovering the 12-fold symmetry. About the peculiarity of sensitivity to twist angles in this system, Shen *et al.* had a detailed discussion. They found that further twist near 30° could result in drastically distinct electron behaviors for left- and right-twisted cases.[99] They pointed out that dielectric response of the left-twisted case will be suppressed while that of the right-twisted case will witness an amplification. Such differences can be attributed to redistribution of charge arising from stacking orders due to twist, which generates twist-dependent pseudospin textures. Similar investigation was also

reported in twisted double bilayer graphene by Yu *et al.*,[100] they found "12-fold-symmetry-like" states with reduced symmetry compared with those in 30° quasi-crystalline TBG.

Then for interlayer conductance, Koren *et al.* found two prominent peaks at twist angles 21.8° and 38.2° for relatively twisted graphite bulks. The explanation involves SE symmetry analysis of the twisted interface. For SE-odd stacking symmetry, the coupling of the two layers' Dirac cones with the assistance of the reciprocal superlattice vectors will give rise to two gapped and two touching massive Dirac bands situated at a specific point in MBZ [Fig. 11(e)]. For SE-even stacking symmetry, a small gap is found in the massive Dirac bands. In addition, no peaks are found at twist 27.8° and 32.2° although there are two peaks in theoretical calculation. The reason may be the relatively weak interlayer coupling, further indicating that the coupling is really subtle and delicate.[97]

Another experiment by Pal *et al.* reveals something interesting about special twist angle 38.2°. They found that at a relatively large twist angle (38.21°), the interlayer coupling will become very strong, resulting in the localization of electrons within a large scale. This kind of geometric frustration generates completely flat bands. The electron localization of the system at 38.21° is kagome patterned (the pattern is triangular at small twist angles), which has a close relation to the spin-liquid. In addition, the modification of the electronic structure at 38.21° is essentially distinct from that under small twist angles, and the low-energy physics of this system has an exact analytic solution. According to the solution of the low-energy structure, the spectrum comprises a pair of triplets, each of which contains two dispersive bands and a flat band.[101]

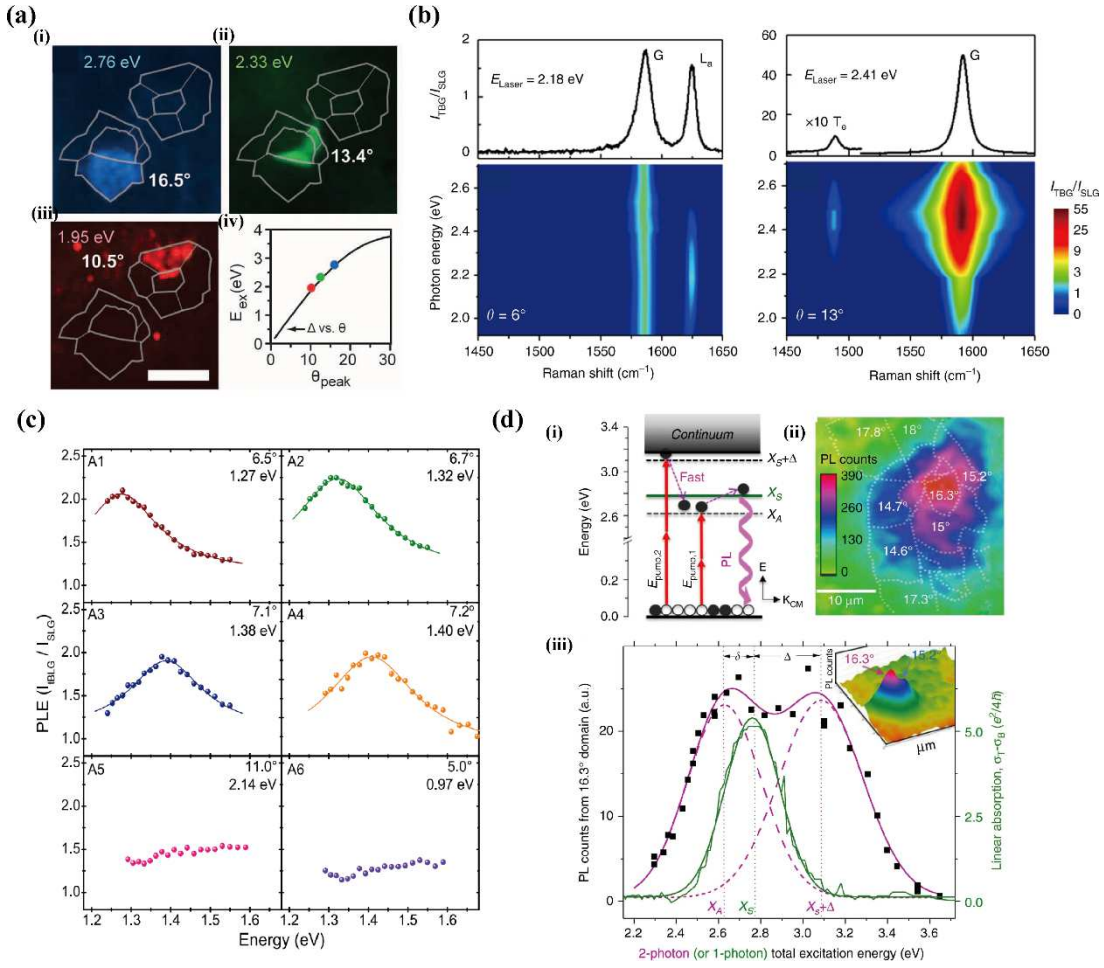

Fig. 12. (a) (i–iii) The intensity of G Raman band imaging of TBG on the SiO_2/Si substrate with excitation energies of 2.76, 2.33, and 1.95 eV. (iv) The excitation energy as a function of the twist angle where the G band is greatly enhanced (reproduced with permission from Ref. [71]). (b) Raman spectrum of TBG with 6° and 13° twist angles under the different excitation lasers (reproduced with permission from Ref. [102]). (c) The ratio of PL intensity in TBG and SLG as a function of excitation energy (reproduced with permission from Ref. [103]). (d) Exciton model diagram to measure E_b. (ii) Two-photon PL map of TBG with different twist angles. (iii) Two-photon PL spectra (black squares) and 1-photon linear absorption spectra (green line) (reproduced with permission from Ref. [104]).

5.2. Flat Band and Magic Angle. Based on the continuum model we get in the above [Eq. (10)], we can add cut-off and then diagonalize the Hamiltonian to obtain the energy dispersion along a specific path within the MBZ. As displayed in Fig. 2(g), the band structure of 5° TBG has been realized. Dispersive bands which resemble that of SLG can be identified in low-energy range clearly while complicated features emerge in the higher energy zone due to band folding effects.

This band folding effect will actually have a profound influence on the Raman spectra of TBG. For instance, in TBG, the G band of Raman spectra is allowed to participate in the double resonance Raman (DRR) process because of the complicated features of TBG's electronic structure in the high energy range. Resultantly, the G band intensity is much stronger than that in SLG.[71,105] Figure 12(a) shows the enhancement peak as a function of twist angle. Kim *et al.* and Sato *et al.* thought that the enhancement may result from the electron-hole excitation near the VHSs[70,106] [Fig. 6(d)]. This enhancement is controlled by joint density of states (JDOS) and the optical transition matrix element, and can be described as a formula by using the second-order time-dependent perturbation theory. For interlayer JDOS in Ref. [71], there is a singularity in TBG because there are many allowable parallel transitions where the valance band of one layer is parallel to the conduction band of the other layer due to the linearity of Dirac cones [Fig. 6(e)]. However, for the optical transition matrix element, the intralayer transitions are suppressed near VHSs, which means that the DRR process for G band enhancement in TBG is weaker near the VHSs. The parallel transitions are optically active and their strength reaches their maximum near VHSs and decrease progressively at points away from it. The JDOS and optical matrix analysis predict a considerable increase in both Raman intensity and absorption.

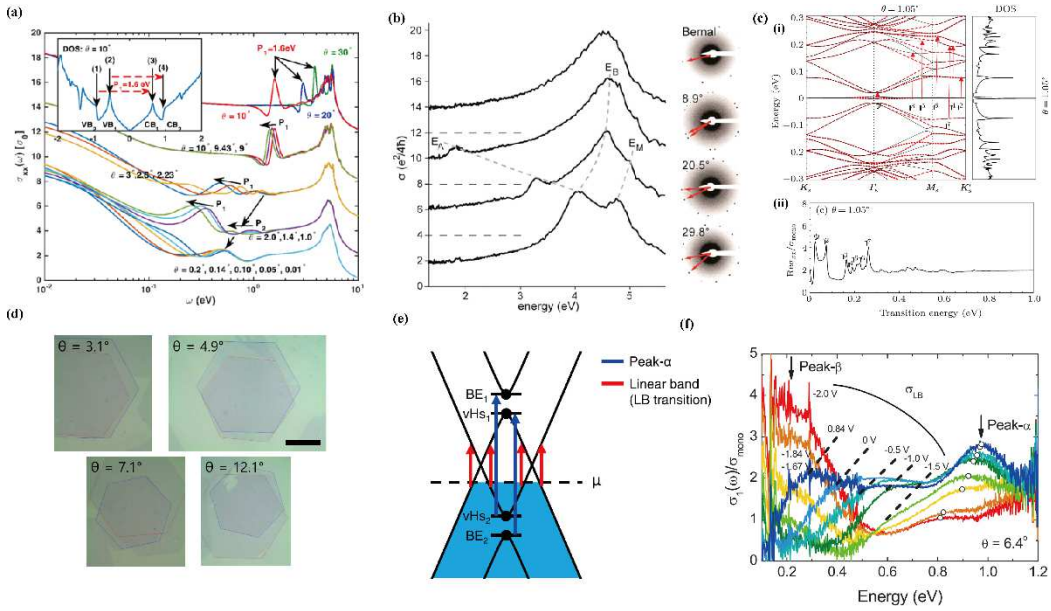

Fig. 13. (a) Optical conductivity of TBG in the twist angle range from 0.01° to 30° (reproduced with permission from Ref. [107]). (b) Measured optical conductivity spectra of MLG and TBG with 8.9°, 20.5°, and 29.8° twist angles. Inset is the electron diffraction image (reproduced with permission from Ref. [108]). (c) (i) Band structure and density of states in TBG with 1.05° twist angle. (ii) Calculated optical conductivity in TBG with 1.05° twist angle (reproduced with permission from Ref. [109]). (d) Optical image of CVD grown TBG with 3.1°, 4.9°, 7.1°, and 12.1° twist angles on the SiO_2/Si substrate. (e) Schematic diagram of TBG's electronic band. Red arrow indicates the linear band transition, and blue arrow indicates the interlayer band transition. (f) Ion-gel gated optical conductivity of TBG with 6.4° twist angle. [(d)–(f)] Reproduced with permission from Ref. [110].

Numerical results of DOS for the TBG system with different twist angles can be obtained as shown in Fig. 2(f). The main feature of this picture is that when twist angle decreases, two symmetry peaks are brought to lower energy range, indicating the suppression of the energy scale of the whole system. Hence, interesting phenomenon appears for tiny twist angles where the merging of two peaks could happen, generating a salient peak in the DOS spectrum due to dense population of states within this range, which corresponds to the flat band in the electronic structure. Accordingly, the movement of the peaks corresponds to shift of VHSs in TBG. The dependence of energy separation between VHSs ($\Delta E_{\rm VHS}$) on the twist angle can be readily derived owing to the linearity of dispersion near two Dirac cones.[40,111,112] Therefore, the smaller the twist angle, the bigger the moiré superlattice, then the smaller the $\Delta E_{\rm VHS}$.[70] This angle de-

pendence leads to several peaks in optical conductivity spectrum of TBG, which results from the electron transition between VHSs, changing their positions as twist angle varies[107] [Fig. 13(a)]. Further investigation proceeded by the microscopic Fourier transform infrared (FTIR) device proved this relation and provide a method of tuning the electronic structure and optical conductivity of TBG by gate voltage[110] [Fig. 13(f)]. A similar experiment about optical absorption spectrum by Havener *et al.*[108] revealed that the absorption peak is also determined by the VHSs in TBG. However, at a large twist angle, the experimental data is not consistent with the theoretical data calculated by the tight-binding model. Through further calculation, the theoretical data showed that the excitonic effect has an impact on the optical absorption spectra of TBG.

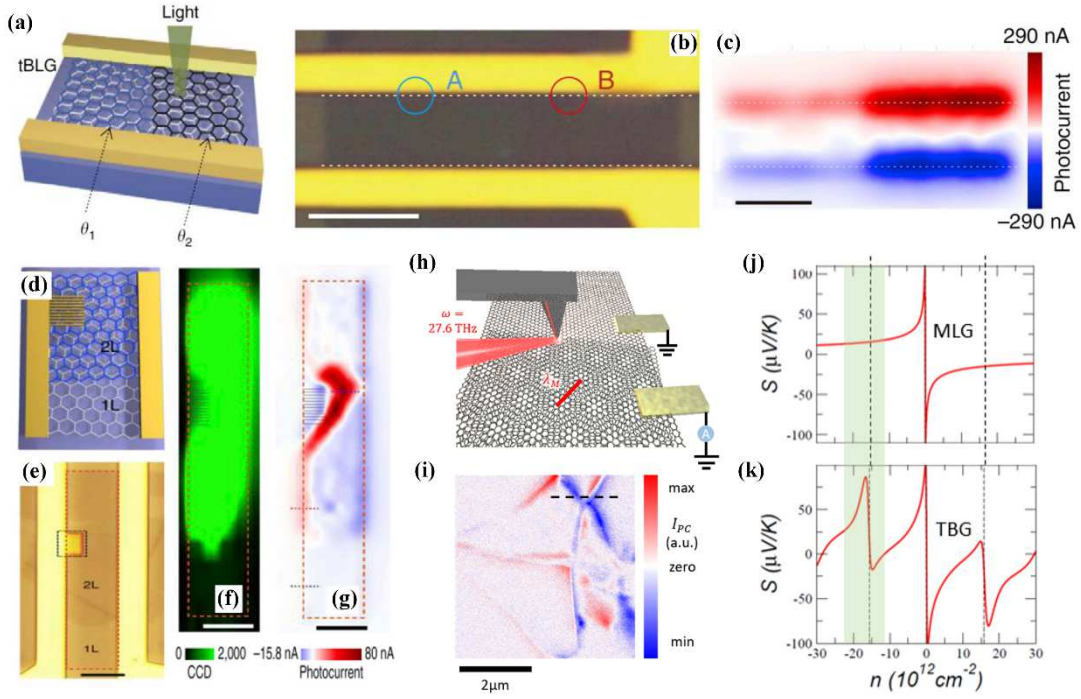

Fig. 14. (a) Scheme of a CVD-based twisted graphene photodetector. (b) Optical image of a CVD-based twisted graphene photodetector. (c) Photocurrent response distribution of the photodetector for different torsion angle ranges. (d) Schematic of the twisted graphene photodetector with attached finger structure. (e) Optical image of the twisted graphene photodetectors with an attached finger structure. (f) Raman G-band intensity distribution of the twisted graphene photodetector. (g) Scanning photocurrent image of the twisted graphene photodetector. [(h), (i)] Schematic diagram of a scanning photocurrent microscope and a photocurrent distribution diagram on the surface of a twisted graphene device. [(j), (k)] Calculated result of the Seebeck coefficient of the single-layer graphene region and the twisted graphene region as a function of the carrier density. (a)–(g) Reproduced with permission from Ref. [96]. (h)–(k) Reproduced with permission from Ref. [113].

Additionally, due to this attractive property of tunability in TBG, researchers began to study optoelectronic devices based on twisted graphene. In 2016, Yin *et al.* prepared a photodetector by stacking CVD twisted graphene.[96] Figures 14(a) and 14(b) show the schematic and optical image of this detector. In the experiment, they demonstrated the selective enhancement of the photoelectric signal of the graphene with a specific twist angle to the laser wavelength. Figure 14(c) shows the photocurrent response distribution of the photodetector for different torsion angle regions. To improve the photoelectric response of the device, they combined a metal plasma nanostructure on the detector, and obtained nearly 80 times the photocurrent enhancement. Figures 14(d) and 14(e) show the detector after adding metal plasma nanostructures. Figures 14(f) and 14(g) show the Raman spectrum map and photocurrent distribution. In 2020, researchers have obtained high-precision photoelectric signal distribution of twisted graphene through scanning photocurrent microscopy.[113] In the experiment, it was found that at the interface of single-layer graphene and twisted graphene, the photocurrent signal was significantly enhanced. Figures 14(h) and 14(i) show a schematic diagram of a scanning photocurrent microscope and a photocurrent distribution diagram on the surface of a twisted graphene device. Further studies have shown that this response stems from the difference in Seebeck coefficient between single-layer graphene and twisted graphene under different carrier concentrations. Figures 14(j) and 14(k) show the calculated result of the Seebeck coeffi-

cient of the single-layer graphene region and the tested graphene region as a function of the carrier density. Appealing properties arising from twist angle have received widespread attention from scientists and are usually used in spectroscopy experiments and optical-electronic device designs.[96,114]

However, $\Delta E_{\rm VHS}$ can be affected by corrugation in TBG, decreasing as the ripple increases.[115] The existence of VHSs can lead to selectively enhanced photocurrent generation when incident photons match $\Delta E_{\rm VHS}$[96] [Fig. 11(d)]. When the TBG system is doped to half-moiré-band filling condition, conduction VHS can split up induced by correlation.[116]

The critical angle for the appearance of the flat band can be around 1.5° based on the investigation of Suárez *et al.*, which is also indicative of the depletion of band velocity. This critical angle is widely referred to as the 'magic angle'. De Trambly *et al.* stated that a formula of magic angle where the flat band appears can be obtained based on the so-called 'hard-wall' model which describes the phase accumulation in the reflection at the boundary of the AA-stacked regions.[117] By combining low-energy microscopy and the nano-ARPES method, electronic structure of TBG can be directly observed, which confirms the existence of flat band separated from dispersive high energy bands [Figs. 11(c) and 11(f)].[34,98]

Kinetic energy quenching of electrons at small twist angles puts Coulomb interactions under the spotlight because of its dominance in the formation of correlated states. Relevant research summarized by Ren *et al.* found out that Coulomb interactions may result in spatial redistribution of DOS within each moiré superlattice of TBG by breaking the symmetry of wavefunctions, which can be observed by low-energy conductance maps. Also, pronounced band splitting together appears with the broadening of both flat bands when the flat bands are partially occupied. This phenomenon resembles the quantum Hall ferromagnets in Landau levels of the graphene monolayer, which is highly relevant to strong interactions between electrons.[118] About the appearance of flat band, there are multiple explanations. Suárez *et al.* thought that it originates from the electron confinement in each layer because of the decoupling of two layers[119] while others thought that it is due to the localized states in AA-stacked regions.[44,48,117] There is also a view held by Moon and Koshino *et al.* that the energy scale of the band is proportional to the size of the MBZ and thus the band velocity is suppressed due to the reduced size of MBZ.[120] In addition, there is another standpoint held by Tarnopolsky *et al.*, which relates the flat band to the lowest Landau level in quantum Hall effect on torus.[121] This view is based on an exquisite calculation of the wavefunction. Researchers are also developing new methods to investigate the interaction in TBG, including the efficient quantum Monte Carlo method.[122] This method is helpful for launching comprehensive studies on electronic states in TBG under different filling conditions.

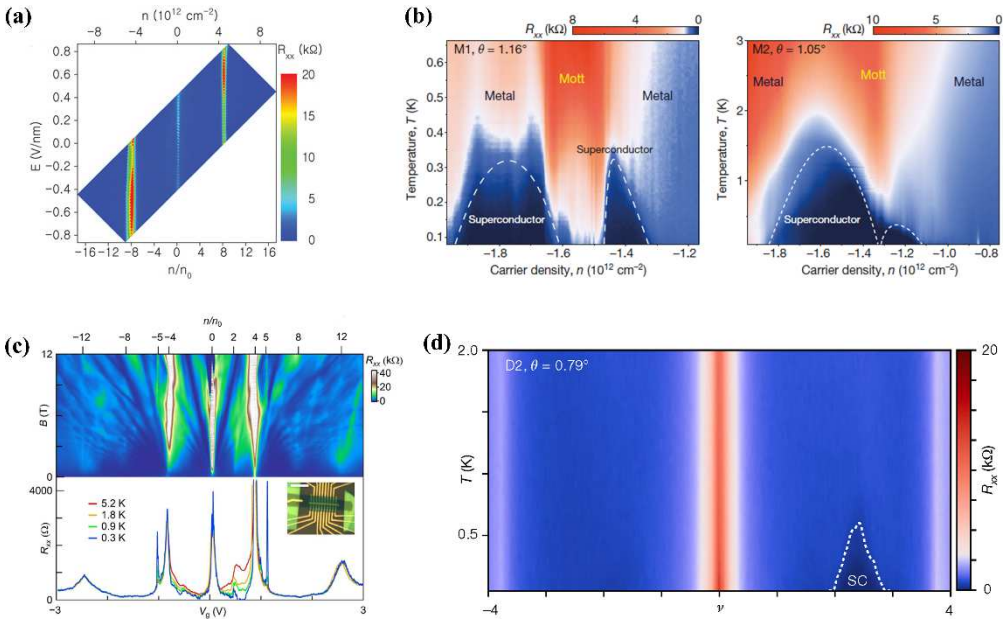

Fig. 15. Longitudinal resistance of TBG as a function of carrier density and transverse electric field (a), carrier density and temperature [(b), (d)], carrier density and magnetic field (c). Two prominent peaks situated at $\pm 4n_0$ are clearly seen in (a) from 0.97° TBG (reproduced with permission from Ref. [47]). Superconducting domes and Mott-like correlated insulating regimes can be obviously found in (b) for two different devices (reproduced with permission from Ref. [35]). Four noticeable peaks at $\pm 5n_0$ and $\pm 12n_0$ are pronounced in (c) for 0.93° TBG (reproduced with permission from Ref. [23]). Stabilized superconducting dome can be obtained in TBG with a lower twist angle after the insertion of WSe_2 layer, as shown in (d) (reproduced with permission from Ref. [123]).

5.3. Magic Angle Twisted Bilayer Graphene. Conductivity minimum can usually be found at neutrality because of the vanishing DOS. However, at satellite densities such as ±8 electrons per moiré supercell of TBG, there are also minima of conductivity and meanwhile, an external electric field imposed on TBG will not weaken the conductivity minimum at neutrality[47] [Fig. 15(a)].

Similarly, when there is an integer number of electrons in the moiré superlattice, TBG usually exhibits insulating states.[118] Yan *et al.* argued that if the Fermi level can be raised to the neighborhood of a saddle point at a certain twist angle, it is possible to realize superconductivity.[112] Cao *et al.* found that magic angle twisted bilayer graphene (MATBG) with ∼1.1° twist angle will become an unconventional superconductor when slightly doped away from the half-filling condition. Properties of this superconductor rely on temperature and intensity of the external magnetic field.[35] Superconducting domes flanked the correlated Mott-like insulating states as labeled in Fig. 15(b). Although argued to be Mott-like insulating states, this correlated insulator is more like a spin-density-wave (SDW) phase resulting from electron instabilities, which is properly described by Liu *et al.*[124] based on a tight-binding model and random phase approximation with $p_{x,y}$ Wannier orbitals and well reconstructed hopping integral taken into account. The asymmetry of superconductivity with respect to carrier density is also included. Another five-band model provides more accurate details of topological and electronic properties than a two-band model,[125] which especially emphasize the effect of "inter-valley Hund's rule exchange interaction". This interaction will break the degeneracy between charge-density wave (CDW) and SDW, leading to either CDW- or SDW-dominant mixed orders, which specifically depends on the sign of interaction coefficient. Due to the fact that these Mott-like insulating states actually behave differently from Mott insulators, we would like to refer to them as correlated insulators in the following.

The discovery of superconductor astonishes and interests many researchers because TBG could be an essential platform to understand superconducting mechanisms which, nevertheless, does not need complicated manipulation but just misalignment between two layers. Then similar superconductivity and correlated insulating states were reported by Codecido *et al.* at 0.93° TBG, an angle smaller than that in Ref. [35]. There are two resistance peaks observed at 5 electrons/holes per moiré unit cell, which are theoretically believed to originate from the flat regions of high energy bands [Fig. 15(c)]. Other prominent resistance peaks are also found at 12 electrons/holes per moiré unit cell, which may result from the existence of satellite Dirac points in the high-energy range.[23] Interestingly, Arora *et al.* found that insertion of one layer of WSe_2 between hBN and TBG can change the microscopic dielectric environment, which leads to more stable superconductivity at a smaller twist angle [∼0.79°, Fig. 15(d)].[123]

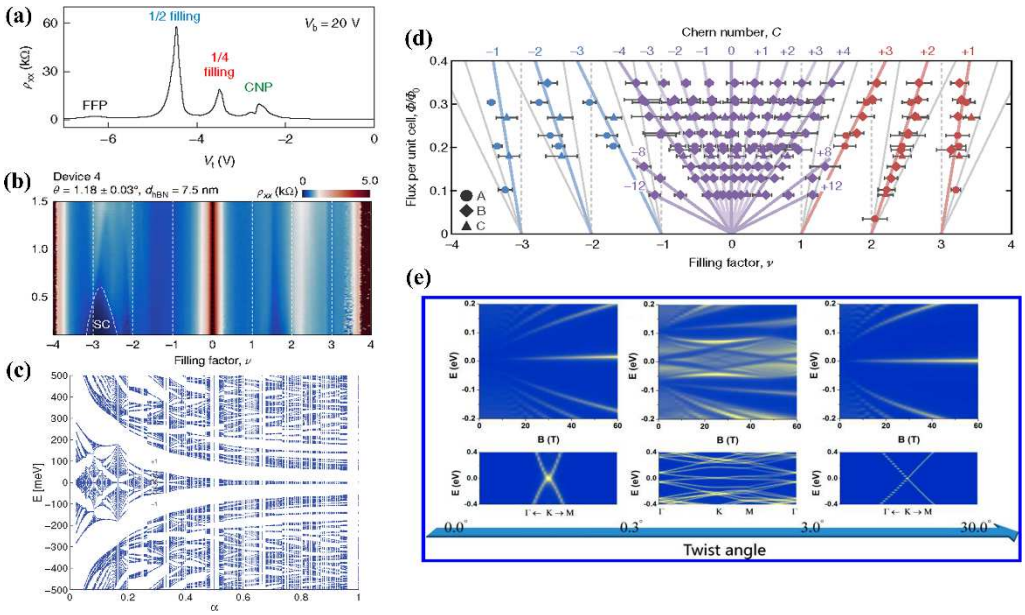

Fig. 16. (a) Resistivity of ABC-trilayer graphene on hBN under gate voltage of 20 V, where two peaks are found at half and quarter filling (reproduced with permission from Ref. [126]). (b) Isolated superconducting dome in 1.18° TBG at appropriate thickness of hBN gate (reproduced with permission from Ref. [127]). (c) Hofstadter-like sub-band structure of TBG (reproduced with permission from Ref. [128]). (d) Relationship between filling factor and Chern insulator with different Chern numbers for three different devices (reproduced with permission from Ref. [129]). (e) Electronic structure and Landau level diagram of TBG with different twist angles (reproduced with permission from Ref. [130]).

Further investigations showed that correlated insulating states can be observed at 1/4 and 1/2 filling of the miniband in the ABC trilayer situated on hBN [Fig. 16(a)]. This type of tunable correlated insulator has acute sensitivity to vertical electrical field and electrostatic gating which modulate the band gap and the electron doping, respectively. The reason for this phenomenon could be the interplay between the cubic energy dispersion in the electronic spectrum of ABC trilayer graphene and the narrow electronic mini bands resulting from the moiré potential.[126] The emergence of correlated insulating states in this system stresses the vital role of moiré potential in the following experiment where superconducting domes are observed near the correlated states.[131]

Ge *et al.* studied the moiré potential arising from lattice mismatch between graphene and hBN and revealed that in the graphene/hBN/graphene sandwiched structure, interlayer electron transport is influenced by the relative rotation of the hBN layer when the graphene layers are aligned. This effect is relevant to multiple physical mechanisms controlled by twist angle, Fermi level and bias. For large twist angles ($\theta > 4^\circ$), the resistance, which monotonically increases with the angle, mainly depends on the effective hBN band gap sensed by an electron at the K point of the graphene. The variation of resistance could be up to several orders of magnitude. For small twist angles, non-monotonic features of resistance are found as new conductance channels are opened up by Umklapp processes.[132]

The strong correlation can also break the time-reversal symmetry in TBG, leading to topological insulating phases with Chern number $\pm1, \pm2, \pm3$, which appear at filling factors $\pm3, \pm2, \pm1$, respectively[129] [Fig. 16(d)]. Similarly, in TBG near the magic angle, for filling factor ν, the emergence of topological insulating states with Chern number $|C| = 4 - |\nu|$ at the hole side is also observed. When the twist angle increases further, the Chern insulator will transform into a fractal Hofstadter butterfly quantum Hall insulator.[133]

The above research showed that when moiré bands are partially filled, significant effects on the shape of band structures can appear, thus affecting the electronic properties including Chern number, insulating and superconducting states. Andrei and MacDonald stressed in their review that partial filling of the flat band can break the rotational symmetry of the moiré supercell, thus altering the charge distribution, which results in the nematic state (order) and the stripe-like charge distribution. The view that nematic order may be regarded as an essential precursor to the superconducting states can be supported by some evidence showing the nematic superconducting state.[134]

There are two views about the relation between superconducting states and insulating states, one is that they are connected because the superconducting states usually appear near the insulating state and the superconductivity exhibits an anisotropic response to the direction of in-plane magnetic fields, the other is that they are competing with each other because of the robust existence of superconductivity and even take over in phase space vacated by the correlated insulators.[118] Saito *et al.* found that in TBG, superconductivity can emerge far away from the insulating states and even survive at larger twist angles, which means that it is very possible that superconductivity and insulator result from different mechanisms and compete with each other as mentioned above[127] [Fig. 16(b)].

In addition to transport properties of TBG, researchers are also interested in TBG's behaviors under the magnetic field. Actually, for behaviors of graphene-based system under a magnetic field, there was a summation given by Rozhkov *et al.*, who pointed out that, for SLG, the energy scale of cyclotron is different from that of ordinary 2D gas of massive non-relativistic electrons, which implies that quantum Hall effect (QHE) is accessible at room temperature. A zero-level state exists in SLG, and all of the levels are fourfold degenerate, two from valleys and two from spins. The plateau of QHE in SLG appears at half-integer values of $2e^2/\pi\hbar$, which results from the existence of the level situated at zero energy, contributing to $2e^2/\pi\hbar$ at half-filling. For AA-stacked bilayer graphene under bias voltage, the Landau spectrum is simply two replicas of SLG separated from each other due to the bias. All Landau levels are also fourfold degenerate. The magneto-optical absorption spectra of AB-stacked graphene is rather different because its response to the magnetic field and bias voltage is affected by its gap-opening property.[135] In TBG, nevertheless, things can be very different. Benefited from the large area of a single moiré unit cell, QHE and fractal patterns resembling Hofstadter butterfly can be accessible under the moderate magnetic field[128,136] [Figs. 16(c) and 16(e)]. At a large twist angle, the Landau level spectrum of TBG is similar to that of SLG. At a small twist angle where the coupling is the strongest, the spectrum resembles that of AB-stacked bilayer graphene. While at intermediate angles, the electronic structure contains flat localized states around the Fermi level, thus exhibiting a complicated fractal Hofstadter butterfly pattern.[130] It is found that fractional QHE with filling factor $\nu = \pm5/3$ in capacitance measurements suggests the existence of a finite gap at the original Dirac points.[137]

Wide and deep research has been carried out not only in electro-magnetic experiments but also in optical investigations. Mao *et al.*[63] used two semiconductor membranes to fabricate MATBG-like lattices

with a 2.65° twist angle, which is referred to as optical magic-angle twist bilayer graphene (OMTBG). The Bloch modes in each membrane form the flat band modes, and are tuned to the Dirac point due to the interlayer coupling. The flat band means that the light is stopped and highly localized, which provides a nanocavity for the laser. They used a laser with large optical spot to pump the OMTBG laser, and the OMTBG laser with 1.5 μm was observed in experiment. For plasmonic properties of TBG, based on the direct observation of plasmon polarization at the subwavelength in graphene[138,139] by utilizing a scattering-type scanning near-field optical microscope (s-SNOM) method, other researchers presented further investigations.[140] Hu *et al.*[141] performed the nano-infrared imaging study of the plasmon polarization in CVD-grown TBG and found that the plasmons polarization in TBG varies with the twist angle. In addition, hyperbolic metasurfaces (HMTSs) can be realized by the nanostructured van der Waals materials[142] and graphene nanoribbons.[143] Hu *et al.*[144] theoretically studied the moiré metasurfaces prepared by stacking two graphene narrow ribbons together. They found that when the twist angle is zero, the dispersion contour of the plasmons polarizations is hyperbolic, but it changes to be elliptical as the twist angle increases, which yields a plasmon topological transition. As the chern number changes from 2 to 4, a diffractionless and low-loss flat band appears. These developments have profound meaning for further prosperity of twistronics and photonic devices.[145] Wen *et al.* calculated the optical conductivity in MATBG using the continuum effective models, and tight-binding methods.[109] They found some gaps existing between the flat band and other bands when the lattice relaxation exists, and the formation of some peaks exists in the lowest energy. The measurements of these gaps by the optical spectrum may help in further understanding the transport properties and the impact of lattice reconstruction in MATBG.

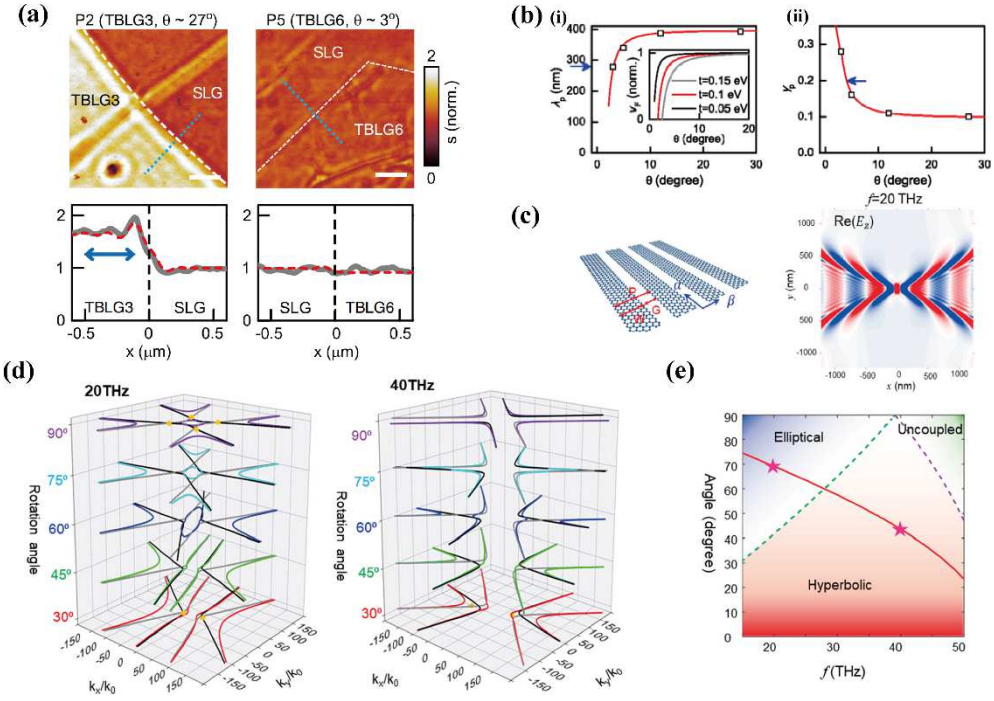

Fig. 17. (a) Near-field amplitude images of MLG and TBG with 3° and 27° twist angles. (b) (i–ii) Wavelength and damping rate of plasmon polarization of TBG as a function of twist angle. [(a), (b)] Reproduced with permission from Ref. [141]. (c) Geometry and polarization dispersion of graphene nanoribbons. (d) Polarization dispersion varied with the twist angle at 20 THz, and 40 THz. (e) Topological transition region as a function of twist angle and frequency. (c)–(e) Reproduced with permission from Ref. [144].

6. Twisted Multilayer Graphene. After the detailed investigations of TBG, we would like to cover some properties and calculations about twisted multilayer graphene (TMG). TMG can be constructed with three or more layers of graphene which, however, could have complicated structures because it can possess no less than two twist angles within the framework. We will mainly introduce three types of TMG and discuss them separately. In the end, we will also concisely mention more complex structures and their properties.

6.1. AB-Stacked Bilayer with One Layer Twisted on Top (ABt Trilayer). The first simple case of TMG is AB-stacked bilayer graphene with one layer twisted relatively on it (ABt trilayer) [Fig. 18(a)]. According to research of Suárez *et al.*, commensurate structure can still be obtained in this situation since the periodicity of AB-stacked graphene is not broken. Actu-

ally, in this case, the continuum model fails to depict the twisted-like band's Dirac point and the gap accurately. Nevertheless, it is able to describe the velocity renormalization properly. Therefore, the tight biding model and the modified continuum model should be adopted in combination to investigate the system. In the tight-binding model, Suárez *et al.* took into account the sublattices which broke the electron-hole symmetry. The band structure comprises parabolic bands with states residing on the AB-stacked bilayer and twisted-like bands with states mainly confined in the twisted single layer. The parabolic bands produce an expansive gap as twist angle decreases. There is also an angle dependence for the twisted-like Dirac point. The renormalization of band velocity of the twisted-like bands is found and band velocity has a tendency to vanish when the twist angle approaches 0. The parabolic band with lowest energy is fixed at zero energy, which reveals its nonbonding character and weak coupling with other bands. Meanwhile, the dependence of energy shifts of other parabolic bands' minimum on the twist angle is also demonstrated [Figs. 18(b) and 18(c)]. In addition, the decrease of twist angle will induce drastic increase of the degree of electron-hole asymmetry. Also, they studied the layer distribution of different states in the band structure. The band pinned at zero energy corresponds to the states located in the outer layer of the AB-stacked bilayer; the shifted parabolic band denotes the states residing in the inner Bernal layer; then the linear twisted-like band stands for the states in the twisted layer. For small angles, the carriers in shifted parabolic band and the linear band have mixed spatial distribution, which indicates the enhancement of coupling. This is also where the velocity renormalization happens. More details can be referred to Ref. [146].

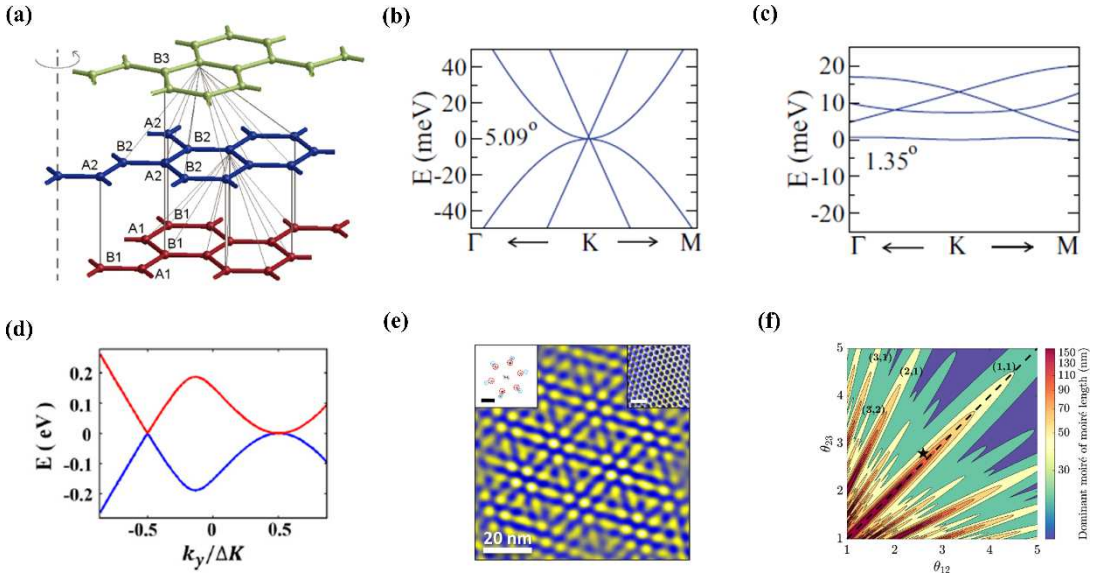

Fig. 18. (a) The geometric structure of ABt trilayer graphene. (b) Band structure of ABt trilayer graphene with twist angle 5.09° along the path $\Gamma \to K \to M$. Dispersive bands and parabolic bands are easily identified. (c) Band structure of 1.35° ABt-trilayer along the same path as in (b). Shift of Dirac point and gap-opening can be observed in this case. (a)–(c) Reproduced with permission from Ref. [146]. (d) Electronic structure of 3.89° ABt trilayer graphene (reproduced with permission from Ref. [147]). (e) STM topography of consecutively twisted trilayer layers (CTTG). Top left inset shows the fast Fourier transform images of STM results. Top right inset shows a 2 nm × 2 nm STM image of CTTG with honeycomb lattice (reproduced with permission from Ref. [36]). (f) Dominant moiré of moiré length for CTTG. The integer pair indicates the harmonic order (reproduced with permission from Ref. [27]).

Correa *et al.* also investigated relevant properties of ABt trilayer, they found that the electronic structure can be analyzed by the combination of the twisted-like and the Bernal-stacking bands. They depicted the dispersion as the intersection of the Bernal-stacking dispersion and the twisted-like dispersion due to a twist angle, which is referred to as a "subvalley" [Fig. 18(d)]. Then, they studied the transmission spectra of the subvalleys. They found that the transmission spectrum of two subvalleys resemble those in a single-layer and in Bernal bilayer graphene, respectively. However, there are some differences, which means that the quasiparticles in subvalleys are not pure massless Dirac fermions or pure massive chiral fermions. They are the compound of the two. For the out-of-lane quantum tunneling, they studied the overlap of the Fermi surface of the twisted-like and the Bernal-stacking bands, which involves the pseudo spin and valley polarization [Fig. 19(d)]. They showed that at large Fermi energy, a magic twisted angle exists, which results in the valley-polarized quantum tunneling. This can be utilized to achieve the valley-polarized quantum tunneling.[147]

For the optical absorption peaks of ABt trilayer,

Correa *et al.* also found that one peak related to the transitions at the K point of the first Brillouin zone shows up, along with the other two peaks that are highly relevant with the VHSs at the M point [Figs. 19(b) and 19(c)]. At a large twist angle, the first peak is situated in the mid-infrared region while appearing in the far infrared region at small twist angles. The latter two peaks experience a shift as the twist angle decreases just like in TBG while visible for large twist angles.[148]

In addition, there is a model developed by Amorim and Castro for the incommensurate structure to describe or predict the spectral quantities including angle resolved photoemission spectroscopy (ARPES) intensity and the total and local densities of states. The model is based on "the expansion of the electronic wavefunction in terms of Bloch waves of individual layers" (page 1). This model can be applied to any incommensurate system theoretically, and it found that the modulation between layer 1 and layer 3 can be important.[149]

6.2. Middle-Layer Twisted Trilayer Graphene. The second relatively simple case is that the middle layer is twisted while the stacking order of bottom and top layers remains [Fig. 19(e)]. Lei *et al.* found that for middle-layer twisted trilayer graphene (MTTG), a decoupled Dirac band exists at all twisted angles due to the mirror symmetry operator's eigenvalues decoupling bands with even and odd parity, which means that dispersionless bands and dispersive bands can coexist in MTTG with a Dirac cone piercing through the flat band. In addition, the first magic angle where the DOS maximizes for these two different stacking systems appears at different values. They also pointed out that MTTG has a mirror symmetry which, however, can be broken by the lateral translations at a fixed orientation, gate electric fields and top-layer twist. When this symmetry is broken by imposing a displacement field, the Dirac cones from outer layers are shifted away from the ones of the middle layer, along with the decrease of the Drude weight, following the movement of the separated Dirac cones. However, as the displacement potential increases, the moving Dirac points touch the edges of other bands, accompanied by the Drude weight moving back to the Dirac point of the middle layers, with the absolute values increased. When both mirror symmetry and C_{3v} symmetries are broken by lateral translations, a phase factor which involves the displacement vector will appear in the tunneling matrix. As a result, the electron and hole flatbands are separated, indicating that a gap between the flat bands will be easily opened.[28] Pictures of results can be referred to Ref. [28].

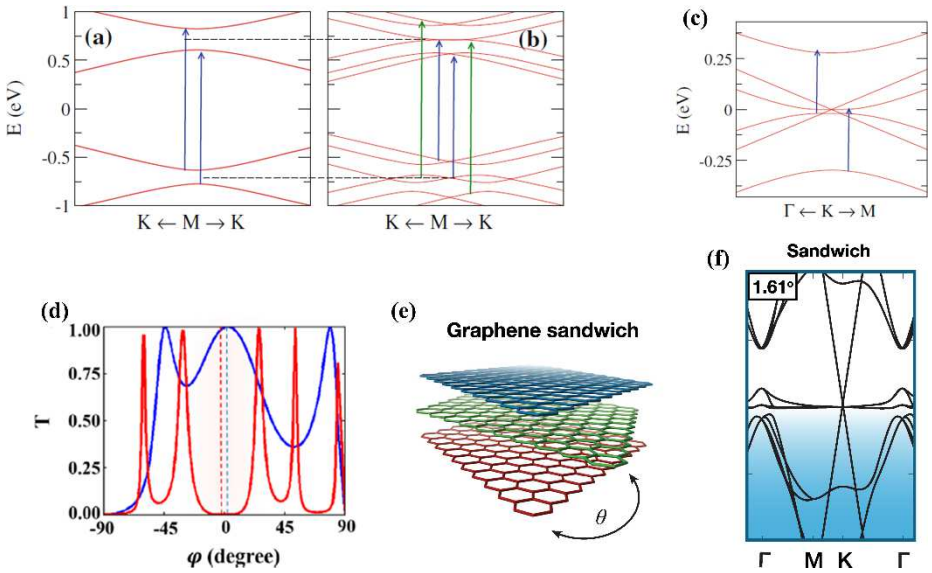

Fig. 19. Comparison of optical transition around the M point of Brillouin zone for TBG (a) and ABt trilayer (b). There are two transition peaks around the M point for ABt trilayer in (b). (c) One single transition peak around the K point for the ABt trilayer. (a)–(c) Reproduced with permission from Ref. [148]. (d) Transmission probability for quasiparticles in two subvalleys of 3.89° ABt trilayer (reproduced with permission from Ref. [147]). (e) Schematic diagram of middle-layer twisted trilayer graphene (MTTG). (f) Band structure of 1.61° MTTG. [(e), (f)] Reproduced with permission from Ref. [29]

Carr *et al.* found that the requirements of the AA alignment of outer layers of MTTG can be naturally satisfied through lattice relaxation process. The external displacement field can modify the energy offset and enhance the coupling between two bands, which could result in correlated states.[29] In addition, Park *et al.* discovered that this kind of twisted trilayer graphene has more flexible tunability of its band structure and superconducting properties than TBG. It is found that there is a close relationship between the ex-

istence of superconductivity and the broken-symmetry phase which originates from two carriers per moiré supercell.[30]

6.3. Twisted Double-Bilayer Graphene. There is another type of twisted multilayer graphene, which comprises two sheets of Bernal-stacked bilayer graphene twisted at the interface relatively [Fig. 20(a)]. Cao *et al.* found that twisted double-bilayer graphene (TDBG) exhibits tunable correlated properties. Its correlated insulator states, which can be switched on and off via displacement field at integer filling of the moiré supercell, are sensitively dependent on the twist angle and the applied displacement field, with the latter dependence revealing the intrinsic polarizability of Bernal-stacked bilayer graphene. TDBG has multiple flat bands in the vicinity of charge neutrality at small twist angles [Fig. 20(b)], which leads to abundant correlated states when each of these flat bands is half filled.[150] Chebrolu *et al.* pointed out that in TDBG, the flat bands can be affected by many factors including twist angle, vertical pressure and interlayer potential differences. It is found that the bandwidths in TDBG are narrower than those in TBG, allowing for greater tolerance of twist angle precision to investigate strongly correlated regime and easier accessibility to narrow band features than in TBG. Pressure can increase the magic angle to larger values while the perpendicular field can influence both the separation between the flat bands and the gap with the higher-energy bands, which can contribute to more effective band isolation. In addition, the interlayer potential difference can also widen the bandwidths. The alignment of bilayer components can also have an impact on the flat bands. TDBG is expected to have narrow bandwidths for a continuous range of twist angle even when the intrinsic gaps are opened by external fields.[151] He *et al.* found that in TDBG, the metallic states near the insulating states witness abrupt decreases in their resistivity when the temperature is lowered. This effect, however, is more likely linked to the spontaneous symmetry breaking because of the simultaneous reversals in the signs of Hall coefficient.[152] Like in TBG, once TDBG is doped away from the half-filled insulating states, superconductivity can be observed, which can be enhanced by in-plane magnetic fields, indicating the existence of spin-polarized electron pairing.[153]

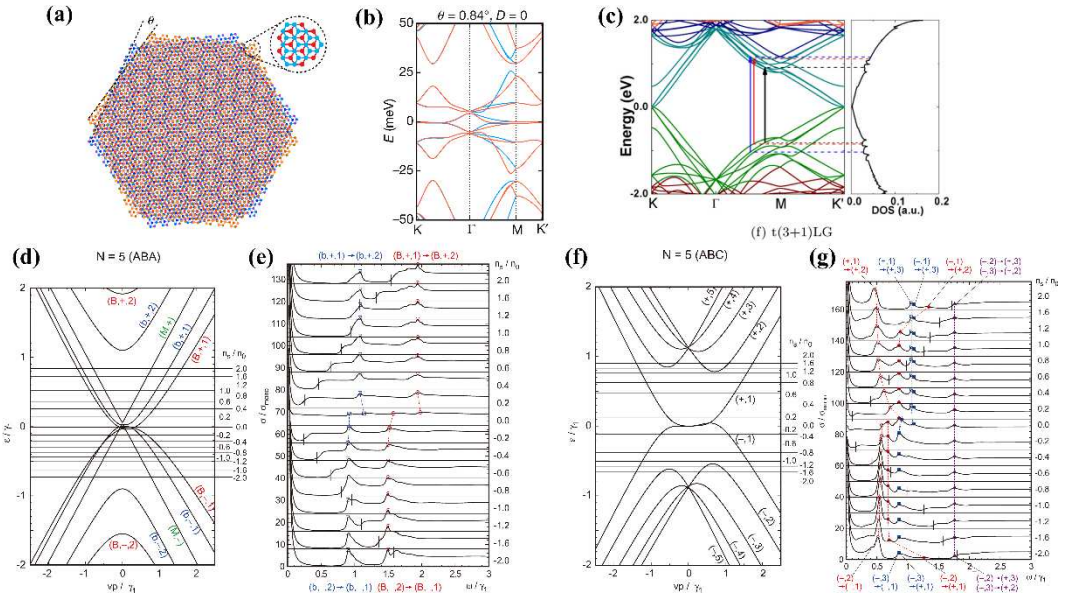

Fig. 20. (a) Schematic diagram of twisted double bilayer graphene (TDBG). (b) Band structure of 0.84° TDBG without bias field. [(a), (b)] Reproduced with permission from Ref. [150]. (c) Band structure and DOS result for one twisted layer on trilayer graphene (reproduced with permission from Ref. [154]). Electronic structure [(d), (f)] and the real part of the dynamical conductivity as a function of frequency ω [(e), (g)] of ABA five-layer graphene, ABC five-layer graphene. (d)–(g) Reproduced with permission from Ref. [155].

6.4. Twisted Multilayer Graphene with More Degrees of Freedom. When there are two different twist angles in TTG, the formed structure will be distinctly sophisticated owing to the lack of periodicity and rise of the "moiré of moiré" pattern. In this structure, Zhu *et al.* found that the moiré pattern formed by the first-second and the second-third twisted layers will consist of a dominant "moiré-of-moiré" supercell lattice [Fig. 18(e)]. This kind of "double moiré pattern" can be distinguished by applying different bias to the sample, just as in the experiment finished by Zuo *et al.*[36]

Actually, there are multiple harmonics which have competing length scales [Fig. 18(f)]. This is the reason why the trilayer system cannot be described by two simple superpositions of TBG. The hybridization

between these two sets of superlattices is pronounced when two angles are equal, which induce the minimal separation between the two lowest VHSs. For general twist angles, the merge of VHSs, which results in DOS peaks and thus, flat band, could occur in a wide range of values. When one of the twist angles is large, then it can be regarded as an effective perturbative potential exerted on TBG.[27] However, Correa *et al.* found that for DOS, the spectrum is similar to two decoupled TBG structures which have two absorption peaks at their respective TBG structure. The positions of these two peaks are dependent on angle. Some properties of the structure, including DOS and optical absorption, just seem like the superposition of two separate TBG structures.[148] This implies that there could be more subtle mechanisms in the properties of the TTG system.

In fact, Vela *et al.* have studied a variety of twisted multilayer graphene systems, which have n-layer Bernal-stacked graphene twisted relatively to m-layer Bernal-stacked graphene, denoted by $t(m+n)$. Their investigation involves the optical analysis of main situations of twisted multilayer graphene including TBG, TTG, TDBG. Also, Fig. 20(c) describes a graphene layer twisted relatively on the top of the trilayer graphene. They found that in all multilayer systems $t(2{+}2)$, $t(1{+}1)$, $t(2{+}1)$, $t(3{+}1)$, k points close to the M point contribute to the largest spectral weights while k points along the Γ–M direction make the most essential contributions to the optical transitions. For $t(1+1)$ and $t(1+1+1)$ systems, a remarkable absorption peak is found for small angles, the energy of which is between $\sim$1 eV and $\sim$2 eV. This peak will witness a shift as the twist angle increases, then split due to enhanced electron-hole asymmetry for intermediate angles. For multilayer complicated systems, an additional infrared optical transition, which does not rely on twist angle, can be observed pronouncedly. The energy of this peak is 0.3, 0.4, 0.5 eV for $t(2{+}1)$, $t(2{+}2)$, $t(3+1)$ systems, respectively. A transition between parabolic bands at the K point generates this peak, which is attributable to the presence of Bernal stacking order in the structure. Theoretically, band anticrossings arouse various allowed optical transitions, which enables a multilayer system to be a suitable platform to observe these transitions. The multilayer system also exhibits a characteristic that the magic angle where the flat band appears is believed to increase as the number of layers increase.[154] Multiple sets of figures can be referred to Ref. [154].

When the number of layers increase further, things become complicated and unresolvable because of the dramatic expansion of degree of freedom if different twist angles should be taken into account. However, there could be some relevant research about different multilayer systems regardless of twist angles which can be referred to. Koshino studied ABA- and ABC-stacked multilayer graphene systems and found that the electronic spectrum and the optical conductivity exhibit different properties [Figs. 20(d)–20(g)]. A model to describe the optical conductivity shows that odd-layered graphene can be regarded as the composition of multi-bilayer-type graphene and one monolayer-type graphene, while even-layered graphene can be regarded as the composition of several bilayers but no monolayer. For absorption spectra of these systems, there are strong peaks in the absorption spectrum of the ABA multilayer, which corresponds to the transitions within separate respective bilayer sub-bands. The appearance of these strong peaks can exist in a wide range of frequency. The main peaks, however, result from the transitions between the zero-energy surface band and excited bands.[155] Systematic investigation can be learnt from Ref. [155].

7. Summary and Outlook. We have introduced the continuum model of TBG which can properly describe the low-energy physics and capture the emergence of flat bands. Then we report recent studies about atomic reconstruction both experimentally and theoretically, which deserve cautious considerations. Comprehensive depiction of this essential structural deformation will be of instructive use for future investigations. We also report relevant observations of the moiré superlattice, which characterize the atomic reconstruction, too. Then we highlight the importance of interlayer coupling in TBG and summarize the experimental observations of correlated insulators and superconductors. We present some optical properties of TBG including G band enhancement, optical conductivity, Umklapp scattering in Raman measurements; chirality, nonlinear properties and plasmons polarization. These discoveries and discussions proved TBG to be an amazing material with intrinsic novel structure which can exhibit various exciting characteristics. We also briefly summarize the progress of twisted multilayer graphene. In the end of this review, we would like to discuss recent advances and new interests.

Mapping of Moiré Superlattices. With the deepening research on twisted graphene, traditional macroscopic detection methods can no longer meet the needs of experiments. A series of visualization methods for moiré pattern developed based on the optical and electrical properties of the moiré superlattice will provide an opportunity to study the unique electronic and atomic structure interactions in the twist system at the nanometer scale. With the help of these methods, researchers can deepen their understanding of the internal physical mechanisms of the twist system such as superconductivity, topological edge states, and correlated insulator phases. What is more, through the effective combination and combined use of moiré pat-

tern visualization technology, researchers can explore in depth more unique properties within the twist system.

Recent Observations in Multilayer Graphene System. The flexibility of stacking gives two-dimensional materials a promising future. Twisted multilayer graphene is a lively example of attempts to discover more appealing properties from complex structures two-dimensional materials could form, which also points to a new direction for two-dimensional materials, that is, endeavor to construct more complicated structures through different combinations in the hope of obtaining more attractive characteristics. Even three-dimensionality can be taken into account to construct van der Waals materials. For instance, recent successful synthesis of twistedly stacked Sb_2Te_3 quintuple layers was reported by Zhou *et al.*, where they found hybridized gaps to be a potential reason for the appearance of quantum spin Hall states.[156] Moreover, the orientations of each layer will be an essential knob to adjust macroscopic properties of the whole system, which endows van der Waals materials with more possibilities to play an adjustable role in future applications. Recently, it is shown that when there are two small independent twist angles in twisted trilayer graphene, zero-resistance domes appear in transport measurements, which is suspect of superconductivity.[157] In addition, twisted trilayer graphene with two independent angles exhibits gapless band structure, which implies that correlated physics could also arise from non-isolated flat bands. This observation could support the view that relative twist would further cause much more complicated properties of van der Waals materials.

Reconsideration of Role of Twist Angles. Recent observations of two kinds of superconductivity in ABC-stacked trilayer graphene implies that interlayer misorientation could not be the requisite reason to obtain superconductor.[158] It enlightens researchers that what really matters in the formation of the unconventional superconductor found in Ref. [158] could be the topology of Fermi surface, Lifshitz transition and isospin-symmetry-broken states[159,160] in trilayer graphene. Therefore, whether or not twist angle should be included in experiments to induce expected superconductivity should be reconsidered.

References

[1] Novoselov K S *et al.* 2004 *Science* **306** 666
[2] Li X and Zhu H 2015 *J. Materiomics* **1** 33
[3] Zhang G *et al.* 2019 *Appl. Phys. Lett.* **114** 253102
[4] Gutiérrez H R *et al.* 2013 *Nano Lett.* **13** 3447
[5] Massicotte M *et al.* 2018 *Nat. Commun.* **9** 1633
[6] Feng J *et al.* 2018 *Nano Lett.* **18** 4493
[7] Brem S *et al.* 2020 *Nanoscale* **12** 11088
[8] Tran K *et al.* 2019 *Nature* **567** 71
[9] Scuri G *et al.* 2020 *Phys. Rev. Lett.* **124** 217403
[10] Ciarrocchi A *et al.* 2019 *Nat. Photon.* **13** 131
[11] Dong X Y *et al.* 2019 *J. Phys. Chem. Solids* **134** 1
[12] Förg M *et al.* 2021 *Nat. Commun.* **12** 1656
[13] Karni O *et al.* 2019 *Phys. Rev. Lett.* **123** 247402
[14] Li A *et al.* 2020 *Chin. Phys. Lett.* **37** 107101
[15] Chu Z *et al.* 2020 *Phys. Rev. Lett.* **125** 186803
[16] Gall M *et al.* 2021 *Nature* **589** 40
[17] Mahapatra P S *et al.* 2020 *Phys. Rev. Lett.* **125** 226802
[18] Mahapatra P S *et al.* 2017 *Nano Lett.* **17** 6822
[19] Regan E C *et al.* 2020 *Nature* **579** 359
[20] Zondiner U *et al.* 2020 *Nature* **582** 203
[21] Bistritzer R and MacDonald A H 2011 *Proc. Natl. Acad. Sci. USA* **108** 12233
[22] Cao Y *et al.* 2018 *Nature* **556** 80
[23] Codecido E *et al.* 2019 *Sci. Adv.* **5** eaaw9770
[24] Lu X *et al.* 2019 *Nature* **574** 653
[25] Wu F and Sarma S D 2019 *Phys. Rev. B* **99** 220507
[26] Lee D S *et al.* 2011 *Phys. Rev. Lett.* **107** 216602
[27] Zhu Z *et al.* 2020 *Phys. Rev. Lett.* **125** 116404
[28] Lei C *et al.* 2021 *Phys. Rev. B* **104** 035139
[29] Carr S *et al.* 2020 *Nano Lett.* **20** 3030
[30] Park J M *et al.* 2021 *Nature* **590** 249
[31] Mora C *et al.* 2019 *Phys. Rev. Lett.* **123** 026402
[32] Xu S *et al.* 2021 *Nat. Phys.* **17** 619
[33] Yoo H *et al.* 2019 *Nat. Mater.* **18** 448
[34] Lisi S *et al.* 2021 *Nat. Phys.* **17** 189
[35] Cao Y *et al.* 2018 *Nature* **556** 43
[36] Zuo W J *et al.* 2018 *Phys. Rev. B* **97** 035440
[37] Goerbig M O 2011 *Rev. Mod. Phys.* **83** 1193
[38] Shallcross S *et al.* 2013 *Phys. Rev. B* **87** 245403
[39] Sboychakov A O *et al.* 2015 *Phys. Rev. B* **92** 075402
[40] Li G *et al.* 2010 *Nat. Phys.* **6** 109
[41] Catarina G *et al.* 2019 *Handbook Graphene Set* (Hoboken NJ: John Wiley & Sons Inc.) vol 3 chap 6 p 177
[42] Mogera U and Kulkarni G U 2020 *Carbon* **156** 470
[43] Nimbalkar A and Kim H 2020 *Nano-Micro Lett.* **12** 126
[44] Dos S J L *et al.* 2012 *Phys. Rev. B* **86** 155449
[45] Shallcross S *et al.* 2008 *Phys. Rev. Lett.* **101** 056803
[46] Yao W *et al.* 2018 *Proc. Natl. Acad. Sci. USA* **115** 6928
[47] Kim K *et al.* 2017 *Proc. Natl. Acad. Sci. USA* **114** 3364
[48] Uchida K *et al.* 2014 *Phys. Rev. B* **90** 155451
[49] Zhang S *et al.* 2020 *Sci. Adv.* **6** eabc5555
[50] Mele E J 2010 *Phys. Rev. B* **81** 161405
[51] Mele E J 2011 *Phys. Rev. B* **84** 235439
[52] Scattering L D 2004 *Molecular Light Scattering and Optical Activity* 2nd edn (Cambridge: Cambridge University Press)
[53] Torsi L *et al.* 2008 *Nat. Mater.* **7** 412
[54] Gohler B *et al.* 2011 *Science* **331** 894
[55] Kim C J *et al.* 2016 *Nat. Nanotechnol.* **11** 520
[56] Matsuo K and Gekko K 2004 *Carbohydr. Res.* **339** 591
[57] Suárez M E *et al.* 2017 *2D Mater.* **4** 035015
[58] Stauber T *et al.* 2018 *Phys. Rev. Lett.* **120** 046801
[59] Addison Z *et al.* 2019 *Phys. Rev. B* **100** 125418
[60] Yang F *et al.* 2020 *Matter* **3** 1361
[61] Malard L M *et al.* 2013 *Phys. Rev. B* **87** 201401
[62] Ha S *et al.* 2021 *Light Sci. Appl.* **10** 19
[63] Mao X R *et al.* 2021 *Nat. Nanotechnol.* **16** 1099
[64] Le S M *et al.* 2019 *2D Mater.* **7** 011005
[65] Lu C C *et al.* 2013 *ACS Nano* **7** 2587
[66] Campos-Delgado J *et al.* 2013 *Nano Res.* **6** 269
[67] Righi A *et al.* 2011 *Phys. Rev. B* **84** 241409
[68] Carozo V *et al.* 2013 *Phys. Rev. B* **88** 085401
[69] Ni Z *et al.* 2008 *Phys. Rev. B* **77** 235403
[70] Sato K *et al.* 2012 *Phys. Rev. B* **86** 125414
[71] Havener R W *et al.* 2012 *Nano Lett.* **12** 3162
[72] dos Santos J M B L *et al.* 2007 *Phys. Rev. Lett.* **99** 256802
[73] de Trambly L G *et al.* 2010 *Nano Lett.* **10** 804
[74] Brihuega I *et al.* 2012 *Phys. Rev. Lett.* **109** 196802
[75] Du J *et al.* 2021 *Chin. Phys. Lett.* **38** 056301
[76] van Wijk M M *et al.* 2015 *2d Mater.* **2** 034010

[77] Carr S *et al.* 2018 *Phys. Rev. B* **98** 224102
[78] Zhou S *et al.* 2015 *Phys. Rev. B* **92** 155438
[79] Nam N N T and Koshino M 2017 *Phys. Rev. B* **96** 075311
[80] Gadelha A C *et al.* 2021 *Nature* **590** 405
[81] Liu Y W *et al.* 2020 *Phys. Rev. Lett.* **125** 236102
[82] Andersen T I *et al.* 2021 *Nat. Mater.* **20** 480
[83] Wong D *et al.* 2015 *Phys. Rev. B* **92** 155409
[84] Bardeen J 1961 *Phys. Rev. Lett.* **6** 57
[85] McGilly L J *et al.* 2020 *Nat. Nanotechnol.* **15** 580
[86] Schmidt H *et al.* 2014 *Nat. Commun.* **5** 5742
[87] Sunku S S *et al.* 2018 *Science* **362** 1153
[88] Hesp N C H *et al.* 2021 *Nat. Commun.* **12** 1640
[89] Yu Z *et al.* 2020 *Small* **16** 1902844
[90] Perebeinos V *et al.* 2012 *Phys. Rev. Lett.* **109** 236604
[91] Kim Y *et al.* 2013 *Phys. Rev. Lett.* **110** 096602
[92] Li H *et al.* 2018 *Ultramicroscopy* **193** 90
[93] Ahn S J *et al.* 2018 *Science* **361** 782
[94] Moon P *et al.* 2019 *Phys. Rev. B* **99** 165430
[95] Yu G *et al.* 2020 *Phys. Rev. B* **102** 045113
[96] Yin J *et al.* 2016 *Nat. Commun.* **7** 10699
[97] Koren E *et al.* 2016 *Nat. Nanotechnol.* **11** 752
[98] Utama M I B *et al.* 2021 *Nat. Phys.* **17** 184
[99] Shen Y H *et al.* 2021 *Chin. Phys. Lett.* **38** 037501
[100] Yu G *et al.* 2020 *Phys. Rev. B* **102** 115123
[101] Pal H K *et al.* 2019 *Phys. Rev. Lett.* **123** 186402
[102] Eliel G S N *et al.* 2018 *Nat. Commun.* **9** 1221
[103] Alencar T V *et al.* 2018 *J. Phys.: Condens. Matter* **30** 175302
[104] Patel H *et al.* 2019 *Nat. Commun.* **10** 1445
[105] Ni Z *et al.* 2009 *Phys. Rev. B* **80** 125404
[106] Kim K *et al.* 2012 *Phys. Rev. Lett.* **108** 246103
[107] Le H A and Do V N 2018 *Phys. Rev. B* **97** 125136
[108] Havener R W *et al.* 2014 *Nano Lett.* **14** 3353
[109] Wen L *et al.* 2021 *Chin. Phys. B* **30** 017303
[110] Yu K *et al.* 2019 *Phys. Rev. B* **99** 241405
[111] Ohta T *et al.* 2012 *Phys. Rev. Lett.* **109** 186807
[112] Yan W *et al.* 2012 *Phys. Rev. Lett.* **109** 126801
[113] Sunku S S *et al.* 2020 *Nano Lett.* **20** 2958
[114] An X *et al.* 2013 *Nano Lett.* **13** 909
[115] Yan W *et al.* 2013 *Nat. Commun.* **4** 2159
[116] Kerelsky A *et al.* 2019 *Nature* **572** 95
[117] de Laissardière G T *et al.* 2012 *Phys. Rev. B* **86** 125413
[118] Ren Y N *et al.* 2020 *Chin. Phys. B* **29** 117303
[119] Suárez M E *et al.* 2010 *Phys. Rev. B* **82** 121407
[120] Moon P and Koshino M 2013 *Phys. Rev. B* **87** 205404
[121] Tarnopolsky G *et al.* 2019 *Phys. Rev. Lett.* **122** 106405
[122] Zhang X *et al.* 2021 *Chin. Phys. Lett.* **38** 077305
[123] Arora H S *et al.* 2020 *Nature* **583** 379
[124] Liu C C *et al.* 2018 *Phys. Rev. Lett.* **121** 217001
[125] Zhang M *et al.* 2020 *Chin. Phys. B* **29** 127102
[126] Chen G *et al.* 2019 *Nat. Phys.* **15** 237
[127] Saito Y *et al.* 2020 *Nat. Phys.* **16** 926
[128] Bistritzer R and MacDonald A H 2011 *Phys. Rev. B* **84** 035440
[129] Nuckolls K P *et al.* 2020 *Nature* **588** 610
[130] Wang Z F *et al.* 2012 *Nano Lett.* **12** 3833
[131] Chen G *et al.* 2019 *Nature* **572** 215
[132] Ge S *et al.* 2017 *Phys. Rev. B* **95** 045303
[133] Shen C *et al.* 2021 *Chin. Phys. Lett.* **38** 047301
[134] Andrei E Y and MacDonald A H 2020 *Nat. Mater.* **19** 1265
[135] Rozhkov A V *et al.* 2016 *Phys. Rep.* **648** 1
[136] Moon P and Koshino M 2012 *Phys. Rev. B* **85** 195458
[137] Yao W *et al.* 2020 *Chin. Phys. B* **29** 127304
[138] Fei Z *et al.* 2012 *Nature* **487** 82
[139] Chen J *et al.* 2012 *Nature* **487** 77
[140] Zhang Q *et al.* 2021 *Nature* **597** 187
[141] Hu F *et al.* 2017 *Phys. Rev. Lett.* **119** 247402
[142] Li P *et al.* 2018 *Science* **359** 892
[143] Gomez-Diaz J S *et al.* 2015 *Phys. Rev. Lett.* **114** 233901
[144] Hu G *et al.* 2020 *Nano Lett.* **20** 3217
[145] Hu G *et al.* 2020 *Nature* **582** 209
[146] Suárez M E *et al.* 2013 *Phys. Rev. B* **87** 125414
[147] Qiao J B and He L 2014 *Phys. Rev. B* **90** 075410
[148] Correa J D *et al.* 2014 *J. Mater. Sci.* **49** 642
[149] Amorim B and Castro E V 2018 arXiv:1807.11909 [cond-mat.mes-hall]
[150] Cao Y *et al.* 2020 *Nature* **583** 215
[151] Chebrolu N R *et al.* 2019 *Phys. Rev. B* **99** 235417
[152] He M *et al.* 2021 *Nat. Phys.* **17** 26
[153] Liu X *et al.* 2020 *Nature* **583** 221
[154] Vela A *et al.* 2018 *Phys. Rev. B* **98** 155135
[155] Koshino M 2013 *New J. Phys.* **15** 015010
[156] Zhou C *et al.* 2021 *Chin. Phys. Lett.* **38** 057307
[157] Zhang X *et al.* 2021 *Phys. Rev. Lett.* **127** 166802
[158] Zhou H *et al.* 2021 *Nature* **598** 434
[159] Zhou H *et al.* 2021 *Nature* **598** 429
[160] Chatterjee S *et al.* 2021 arXiv:2109.00002 [cond-mat.supr-con]